J. Fluid Mech. (2007), *vol.* 572, *pp.* 145–177.
doi:10.1017/S0022112006003545 Printed in the United Kingdom

On the effects of microbubbles on Taylor–Green vortex flow

By ANTONINO FERRANTE AND SAID E. ELGHOBASHI

Department of Mechanical and Aerospace Engineering, University of California, Irvine, CA 92697, USA

(Received 19 December 2005 and in revised form 15 July 2006)

The paper describes a numerical study of the effects of microbubbles on the vorticity dynamics in a Taylor–Green vortex flow (TGV) using the two-fluid approach. The results show that bubbles with a volume fraction $\sim 10^{-2}$ enhance the decay rate of the vorticity at the centre of the vortex. Analysis of the vorticity equation of the bubble-laden flow shows that the local positive velocity divergence of the fluid velocity, $\nabla \cdot \boldsymbol{U}$, created in the vortex core by bubble clustering, is responsible for the vorticity decay. At the centre of the vortex, the vorticity $\omega_c(t)$ decreases nearly linearly with the bubble concentration $C_m(t)$. Similarly, the enstrophy in the core of the vortex, $\omega^2(t)$, decays nearly linearly with $C^2(t)$. The approximate mean-enstrophy equation shows that bubble accumulation in the high-enstrophy core regions produces a positive correlation between ω^2 and $\nabla \cdot \boldsymbol{U}$, which enhances the decay rate of the mean enstrophy.

1. Introduction

We have demonstrated (Ferrante & Elghobashi 2004, 2005) that, in a microbubble-laden spatially developing turbulent boundary layer, the microbubbles create a local positive divergence of the fluid velocity, $\nabla \cdot \boldsymbol{U} > 0$. This positive $\nabla \cdot \boldsymbol{U}$ generates a fluid mean velocity normal to the wall, which, in turn, displaces the quasi-streamwise longitudinal vortical structures away from the wall to a zone of smaller mean shear, thus reducing the enstrophy in these structures. The result is a reduction in both the production of turbulence kinetic energy in the vicinity of the wall and the effectiveness of the sweep events, and hence a diminishing of the wall skin friction.

However, the spatially developing turbulent boundary layer is a complex three-dimensional flow in which the vortical structures, being subjected to strong shear, undergo shape deformation and vorticity (magnitude and direction) modulation even in the absence of microbubbles. The main objective of the present study is to examine the two-way interaction between microbubbles and geometrically well-defined vortical structures whose vorticity direction is invariant and whose magnitude may undergo only negligible modification in the absence of microbubbles. Taylor–Green vortex flow (TGV) is an ideal flow that satisfies our requirements.

We have performed numerical simulations of a two-dimensional TGV laden with microbubbles using the two-fluid (or Eulerian–Eulerian) approach to examine the effects of the microbubbles on the fluid-velocity divergence, $\nabla \cdot \boldsymbol{U}$, and the subsequent modifications of the vorticity field. In order to perform these simulations we developed a novel numerical method to solve the two-fluid equations for bubble-laden flows with an average bubble concentration $C_0 \sim 10^{-2}$.

Our results for bubbles with Stokes number equal to 0.25 and volume fraction 1 % show that the magnitude of the vorticity at the centre of the vortex decays faster than that for single-phase flow. After 20 turnover times of the initial vortex, the magnitude of the vorticity at the centre of the vortex becomes 34 % smaller than that for single-phase flow. Analysis of the vorticity equation for bubble-laden flow shows that the local positive velocity divergence of the fluid velocity, $\nabla \cdot \boldsymbol{U}$, created in the vortex core by bubble clustering, is responsible for the vorticity decay.

Various studies in the literature have discussed the interaction between bubbles and vortices, e.g. Maxey (1987*b*), Ruetsch & Meiburg (1993),Wang & Maxey (1993), Druzhinin & Elghobashi (1998, 2001), Sridhar & Katz (1999), Mazzitelli, Lohse & Toschi (2003) and Djeridi, Gabillet & Billard (2004). However, none of these studies has analysed the effects of microbubbles on TGV or explained the link between $\nabla \cdot \boldsymbol{U}$ and the reduction in vorticity.

The next section provides a description of the governing equations and a summary of the numerical method, whose details are given in Appendix A. Section 3 describes simulation results for a single-phase TGV and for a bubble-laden TGV. This is followed by the concluding remarks and Appendices A and B. Appendix B gives a comparison of the results obtained from two-fluid and Lagrangian simulations of a bubble-laden TGV.

2. Mathematical description

2.1. *Governing equations*

In the present study we adopt the two-fluid (or Eulerian–Eulerian) formulation for the description of bubble-laden flow. This formulation is obtained by volume- or ensemble-averaging the governing conservation equations of two-phase flows. Volume averaging has been employed by Drew (1983), Drew & Passman (1999) and Sirignano (2005), whereas Zhang & Prosperetti (1997) and Marchioro, Tanksley & Prosperetti (1999) used ensemble averaging.

We assume that the bubbles are non-deformable spheres of diameter d_b much smaller than the characteristic length scale of the flow, L_f. The bubble phase is treated as a continuum characterized by its velocity, $V_i(\boldsymbol{x}, t)$, and concentration (or volume fraction)

$$C(\boldsymbol{x}, t) = n(\boldsymbol{x}, t)\, \mathscr{V}_b, \tag{2.1}$$

where $n(\boldsymbol{x}, t)$ is the bubble number density and $\mathscr{V}_b$ is the volume of a single bubble. The continuity and momentum conservation equations of the carrier fluid and bubbles are averaged over a length scale L_{ave} much smaller than L_f,

$$d_b \ll L_{ave} \ll L_f. \tag{2.2}$$

Equation (2.1) is valid for the condition

$$(d_b/2L_n)^2 \ll 1, \tag{2.3}$$

where L_n is the macroscopic length scale of variation the bubble number density in n (Prosperetti & Zhang 1995). Throughout this manuscript we will use, for brevity, the term 'bubbles' to denote 'microbubbles' which satisfy (2.2) and (2.3).

We treat the bubbles as rigid spheres, under the assumption of 'dirty' bubbles, i.e. that in non-purified liquid water the gas–liquid interface is solidified owing to the presence of impurities (Detsch 1991; Rightley & Lasheras 2000). The density of the bubble gas, ρ_b, is assumed to be negligibly small compared with that of the

ν	ω_0	k_x	k_z
10^{-5}	100	2π	2π

TABLE 1. Properties of the carrier flow.

surrounding liquid, ρ, i.e. $\rho_b/\rho \ll 1$. Thus, the bubbles are assumed to be massless rigid spheres. Bubble–bubble interactions are neglected. The bubble equation of motion, (2.7), below, includes the terms representing the carrier-fluid inertia, the added mass, the Stokes drag, the buoyancy (Maxey & Riley 1983; Druzhinin & Elghobashi 1998) and the lift force (Auton 1987). In two-way coupling, the effects of the bubbles on the fluid are taken into account in both the continuity and momentum equations of the fluid, (2.4) and (2.5) below, via the concentration $C(\boldsymbol{x}, t)$ and the bubble–fluid coupling force $f_i(\boldsymbol{x}, t)$. We write the governing equations for a bubble-laden flow (Drew 1983; Zhang & Prosperetti 1997; Drew & Passman 1999; Marchioro *et al.* 1999; Sirignano 2005) as follows:

(i) *carrier-fluid continuity*,

$$\partial_t(1-C) + \partial_j[(1-C)\,U_j] = 0; \tag{2.4}$$

(ii) *carrier-fluid momentum*,

$$\begin{aligned}\partial_t[(1-C)\,U_i] + \partial_j[(1-C)\,U_i\,U_j] \quad &= -(1-C)\partial_i P + \nu\,\partial_j[(1-C)\,(\partial_j\,U_i + \partial_i\,U_j)] \\ &\quad - f_i + (1-C)\,g_i\,;\end{aligned} \tag{2.5}$$

(iii) *bubble-phase continuity*,

$$\partial_t C + \partial_j(C\,V_j) = 0; \tag{2.6}$$

(iii) *bubble-phase momentum*,

$$\frac{\mathrm{d}V_i}{\mathrm{d}t} = 3\frac{\mathrm{D}U_i}{\mathrm{D}t} + \frac{1}{\tau_b}(U_i - V_i + V_{ti}) + [(\boldsymbol{U}-\boldsymbol{V})\times\boldsymbol{\omega}]_i. \tag{2.7}$$

In the above dimensionless equations, $U_i(\boldsymbol{x}, t)$ and $V_i(\boldsymbol{x}, t)$ are the components of the instantaneous fluid (liquid) velocity $\boldsymbol{U}(\boldsymbol{x}, t)$ and the bubble-phase velocity $\boldsymbol{V}(\boldsymbol{x}, t)$, respectively, $P(\boldsymbol{x}, t)$ is the pressure and ν is the dimensionless kinematic viscosity (table 1). The non-dimensionalization of the governing equations (2.4)–(2.7) is performed using a reference velocity $U_{ref} = 1\,\mathrm{m\,s^{-1}}$, a length scale $L_{ref} = 0.1\,\mathrm{m}$ and a fluid density $\rho_{ref} = 10^3\,\mathrm{kg\,m^{-3}}$, such that for the prescribed Reynolds number ($Re = U_{ref}L_{ref}/\nu_{ref} = 1/\nu = 10^5$) the dimensional kinematic viscosity is that of liquid water, i.e. $\nu_{ref} = 10^{-6}\,\mathrm{m^2\,s^{-1}}$. The parameters in tables 1 and 2 have been non-dimensionalized accordingly.

The coupling force $f_i(\boldsymbol{x}, t)$ in (2.5) is calculated according to Druzhinin & Elghobashi (1998) as

$$f_i = -C\left(\frac{\mathrm{D}U_i}{\mathrm{D}t} - g_i\right) \tag{2.8}$$

where g_i is the component of the acceleration due to gravity in the i-direction. In (2.7) and (2.8), $\mathrm{D}/\mathrm{D}t \equiv \partial_t + U_j\,\partial_j$ is the time derivative following a fluid element. In (2.7), $\mathrm{d}/\mathrm{d}t \equiv \partial_t + V_j\,\partial_j$ is the time derivative in a frame moving with the bubble phase, and the bubble response time τ_b is defined according to Stokes drag law as

$$\tau_b = \frac{d_b^2}{36\nu}; \tag{2.9}$$

Case	C_0	St	τ_b $(\times 10^3)$	$d_b(\times 10^4)$
A	0.01	0.25	2.5	9.5
B	0.001	0.25	2.5	9.5
C	0.02	0.25	2.5	9.5
D	0.01	0.1	1.0	6.0
E	0.01	0.5	5.0	13

TABLE 2. Physical parameters for the test cases of the bubble-laden TGV.

V_{ti} is the bubble terminal velocity in a quiescent fluid ($V_{ti} = -2\tau_b\, g_i$). In the present study we set the acceleration due to gravity equal to zero, $g_i = 0$; thus $V_{ti} = 0$.

The last term on the right-hand-side of (2.7) gives the lift force according to Auton (1987); here $\boldsymbol{\omega}(\boldsymbol{x}, t)$ is the vorticity. It should be noted that Auton's expression is for a sphere in an inviscid rotational flow, whereas Saffman's lift force (Saffman 1965) L_i,

$$\frac{L_i}{\frac{1}{2}\,\rho\,\mathscr{V}_b} = \frac{19.38}{\pi d_b}\,[(U_j - V_j)\,(\partial_i U_j)]\,\frac{\nu^{1/2}}{\|\partial_i \boldsymbol{U}\|^{1/2}}, \tag{2.10}$$

is for a sphere in a linear shear at small Reynolds number. Our simulation results indicate that neither lift expression significantly modifies the effects of bubbles on the vorticity of the TGV (figure 7). We thus adopt Auton's in our computations.

For the case of vanishingly small bubble volume fraction ($C \ll 1$) the effects of the bubbles on the carrier fluid are negligible (one-way coupling), and the carrier-fluid continuity and momentum equations, (2.4) and (2.5), reduce to the incompressible Navier–Stokes equations,

$$\partial_j U_j = 0, \tag{2.11}$$

$$\partial_t U_i + \partial_j (U_i\, U_j) = -\partial_i P + \nu\, \partial_j \partial_j U_i + g_i. \tag{2.12}$$

2.2. *Initial and boundary conditions*

The initial fluid-velocity field for two-dimensional Taylor–Green vortex flow (Taylor 1923) is prescribed as follows:

$$\begin{aligned} U_1(\boldsymbol{x}, 0) &= -\omega_0\,\frac{k_z}{k^2}\cos(k_x\, x)\sin(k_z\, z), \\ U_2(\boldsymbol{x}, 0) &= 0, \\ U_3(\boldsymbol{x}, 0) &= \omega_0\,\frac{k_x}{k^2}\sin(k_x\, x)\cos(k_z\, z), \end{aligned} \tag{2.13}$$

where ω_0 is the initial maximum vorticity ($\omega = \partial_z U_1 - \partial_x U_3$), k_x and k_z are the wavenumbers in the x- and z-directions, and $k^2 = k_x^2 + k_z^2$. The dimensionless parameters required to characterize the carrier flow are given in table 1.

The bubble-phase velocity components are set equal to those of the carrier fluid at time $t = 0$:

$$V_i(\boldsymbol{x}, 0) = U_i(\boldsymbol{x}, 0). \tag{2.14}$$

The initial bubble-concentration field is prescribed as a uniform constant throughout the computational domain:

$$C(\boldsymbol{x}, 0) = C_0. \tag{2.15}$$

The values of C_0 and other dimensionless physical parameters for the five test cases studied are given in table 2, where St denotes the Stokes number, defined as

$$St = \tau_b\, \omega_0. \tag{2.16}$$

In cases B, A and C the Stokes number was kept constant ($St = 0.25$) while the bubble volume fractions, C_0, for the three cases were 0.001, 0.01 and 0.02, respectively. In cases D, A and E the bubble volume fraction was kept constant ($C_0 = 0.01$) while the Stokes numbers were 0.1, 0.25 and 0.5, respectively. Case E had the largest bubble diameter among the cases studied, with $d_b \simeq \Delta x/8$ for a computational mesh with uniform grid spacing $\Delta x = 0.01$; thus conditions (2.2) and (2.3) were satisfied in all five test cases A–E. For the prescribed reference length scale $L_{ref} = 0.1$ m, the dimensional bubble diameter is 100 μm in cases A–C, 63 μm in case D and 137 μm in case E.

Periodic boundary conditions are applied in the three spatial directions. Although the flow being studied is two-dimensional we use a three-dimensional computational domain but with only two planes in the y-direction. The results to be presented in § 3 were obtained using a uniform mesh of $96 \times 2 \times 96$ grid points in the x-, y- and z-directions, respectively. The dimensionless lengths of the computational domain were $L_x = L_z = 1$ and $L_y = 2\Delta x$.

2.3. *Numerical method*

The governing equations (2.4)–(2.7) are solved numerically using a newly developed predictor–corrector method similar to that described by Najm, Wyckoff & Knio (1998) for simulating unsteady combustion in two dimensions. The predictor uses a second-order Adams–Bashforth time-integration scheme to time-advance the velocities U_i and V_i and the scalar field C. The corrector uses a second-order Crank–Nicolson time-integration scheme. In order to satisfy the continuity equation of the carrier fluid, (2.4), a Poisson equation for the pressure is solved in both the predictor and corrector steps, and a pressure correction is applied to the velocity field U_i. We use a staggered Cartesian grid where we compute the scalar fields P and C at the cell centres, and the velocity components at the centres of the cell sides. The spatial derivatives in (2.5) and (2.7) are computed via second-order central differencing. In order to ensure the positivity of the scalar field C, the spatial derivatives in (2.6) are computed using a MUSCL-TVD (monotone upstream-centred scheme for conservation laws – total-variation-diminishing) scheme (Van Leer 1979; Hirsch 1990, pp. 552–553) with the 'Superbee' flux-limiter function developed by Roe (1985). Our results show that this numerical scheme conserves the bubble concentration C at all times, as evidenced by the negligible ($<10^{-14}$) absolute value of the error $(C_0 - \langle C \rangle)/C_0$, where $\langle C \rangle$ denotes the instantaneous spatially averaged C over the (x, z)-plane. It should be noted that the lagrangian–eulerian-mapping (LEM) method proposed by Druzhinin & Elghobashi (1998) for the bubble-laden-flow equations with one-way coupling is non-conservative.

Our results for the two-way coupling cases show that the numerical solution obtained using only the predictor steps described in Appendix A is stable until the maximum bubble concentration, $C_m(t)$, reaches approximately 0.25. The additional corrector steps stabilize the solution until $C_m(t)$ reaches 0.5 (figure 16). For the one-way coupling simulations the corrector steps are not required since the numerical solution for one-way coupling, with only the predictor, is stable for large $C_m(t)/C_0$ ratios (figure 6). The details of the numerical method for both two-way and one-way coupling simulations are given in Appendix A. The present two-fluid formulation differs from the Lagrangian method used in our recent papers on microbubble drag reduction (Ferrante & Elghobashi 2004, 2005). An independent validation of either method is lacking at present. Thus, we compare the results of the Lagrangian and two-fluid simulations of the bubble-laden TGV in Appendix B.

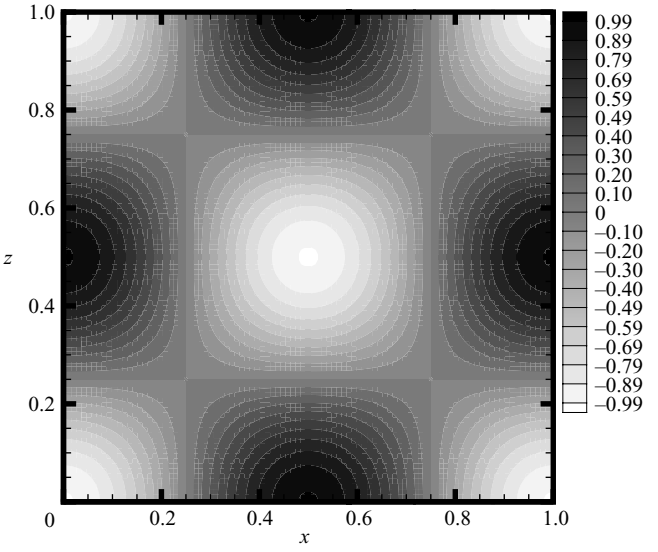

FIGURE 1. Instantaneous contours of the vorticity ω/ω_0 at time $t = 0.2$ in one-way coupling.

3. Results

3.1. *Single-phase Taylor–Green vortex*

The Taylor–Green vortex flow (TGV) is a two-dimensional array of counter-rotating vortices (figure 1), whose vorticity decays in time owing to viscous diffusion ($\partial_t \omega = \nu \nabla^2 \omega$). TGV is an exact solution of the time-dependent incompressible Navier–Stokes equations for a single-phase flow (Taylor 1923). The analytical solution of (2.11), (2.12) with the initial conditions (2.13) gives the instantaneous velocity components as

$$\left.\begin{aligned} U_1(\boldsymbol{x}, t) &= -\omega_0 \frac{k_z}{k^2} \cos(k_x x) \sin(k_z z) \exp(-\nu k^2 t), \\ U_2(\boldsymbol{x}, t) &= 0, \\ U_3(\boldsymbol{x}, t) &= \omega_0 \frac{k_x}{k^2} \sin(k_x x) \cos(k_z z) \exp(-\nu k^2 t)\,. \end{aligned}\right\} \tag{3.1}$$

The corresponding vorticity is

$$\omega(\boldsymbol{x}, t) = \partial_z U_1 - \partial_x U_3 = -\omega_0 \cos(k_x x) \cos(k_z z) \exp(-\nu k^2 t)\,. \tag{3.2}$$

Figure 2 gives the analytical x-profile of ω/ω_0 at $z = 0.5$ and time $t = 0.2$ together with, for comparison, our numerical solution of (2.11) and (2.12) for the initial conditions (2.13). The time $t = 0.2$ equals 20 turnover times of the initial vortex ($\omega_0 = 100$). The figure shows that the analytical and numerical solutions for ω are identical.

3.2. *Bubble-laden Taylor–Green vortex with one-way coupling*

In this section we describe the numerical solution of the governing equations (2.11), (2.12), (2.6) and (2.7) for a bubble-laden TGV with one-way coupling, i.e. the bubbles do not affect the fluid motion.

In § 2.1 we assumed the bubbles to be massless spheres since the density of their gaseous content is much smaller than that of the surrounding liquid. Thus, once bubbles are released in a TGV they move along spiral trajectories (see the dashed arrows in figure 3) towards the nearest vortex centre, mainly owing to their added

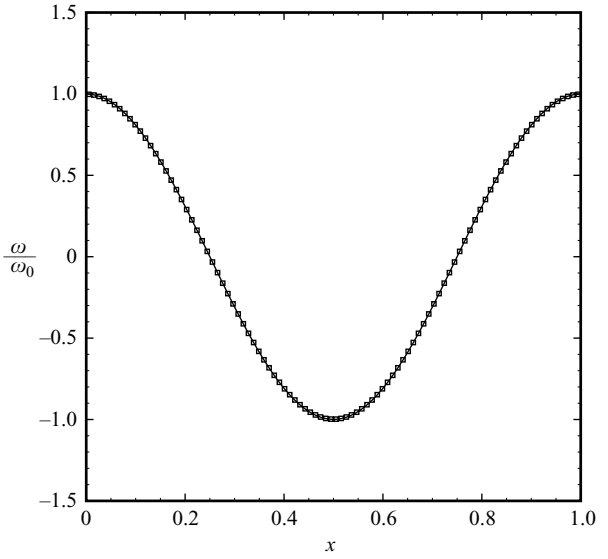

FIGURE 2. Instantaneous x-profile of ω/ω_0 at $z = 0.5$ and time $t = 0.2$ for single-phase TGV: analytical equation, (3.2) (solid line); numerical solution (symbols).

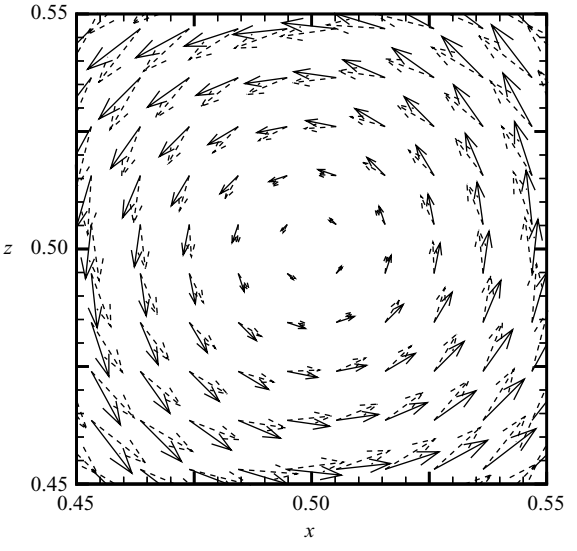

FIGURE 3. Instantaneous velocity vectors for the fluid, $\boldsymbol{U}$ (solid arrows), and bubble phase, $\boldsymbol{V}$ (dashed arrows), at time $t = 0.2$ for case A (with one-way coupling).

mass and the pressure-gradient terms contained in $\mathrm{D}\boldsymbol{U}/\mathrm{D}t$ (figure 4), the first term on the right-hand side in (2.7). Consequently the bubble concentration C increases with time in the high-enstrophy regions and decreases in the low-enstrophy regions (figures 1 and 5). In reality there is a maximum value of C within a finite domain based on the maximum number of spheres that could be packed in a cube. This value ranges from $\pi/4$ in two dimensions to $\pi/6$ in three-dimensions. However, we constrained C only to be positive using the MUSCL-TVD scheme in discretizing the spatial derivatives in (2.6), i.e. we did not prescribe an upper limit for C. The growth

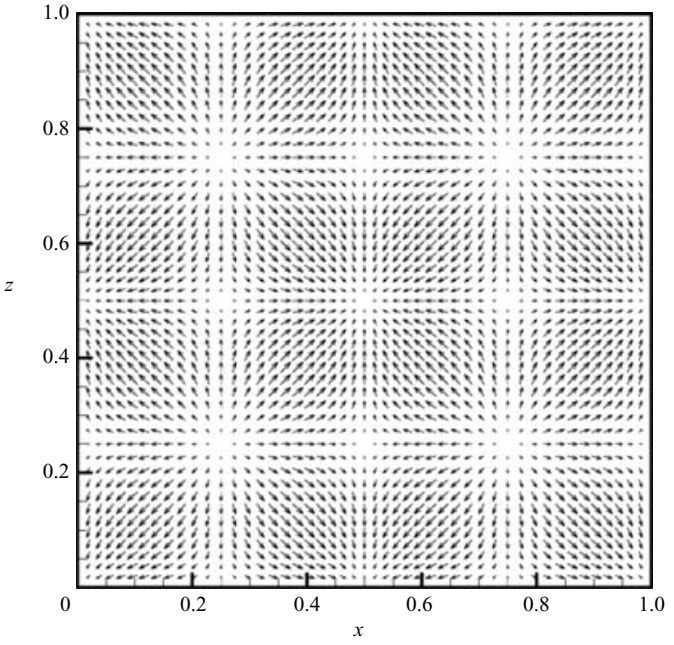

FIGURE 4. Instantaneous $D\boldsymbol{U}/Dt$ vectors at time $t = 0.2$ in a two-dimensional TGV.

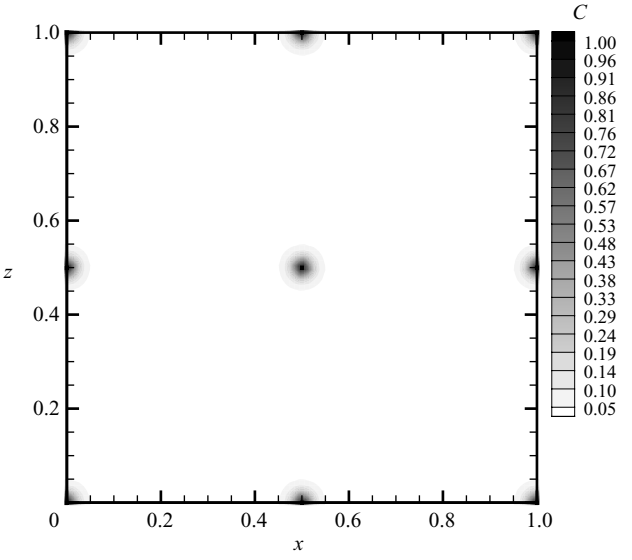

FIGURE 5. Instantaneous contours of the bubble concentration C at time $t = 0.2$ for case A (with one-way coupling).

rate of the maximum concentration, $C_m(t)$, increases with time initially (figure 6), but as bubbles accumulate at the vortex centre the growth rate diminishes and tends to zero asymptotically with time. The following approximate analytical solution for the temporal development of $C_m(t)$ in the case of one-way coupling was derived by Druzhinin & Elghobashi (1998) under the assumption of small Stokes number

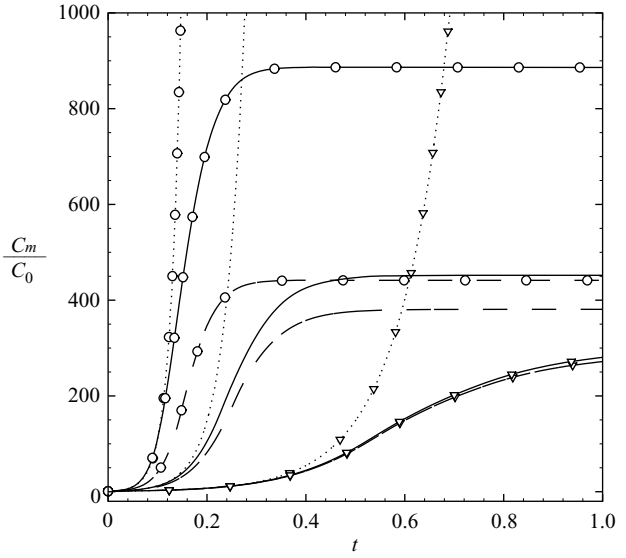

FIGURE 6. Temporal development of C_m/C_0 for cases A–E with one-way coupling. Approximate analytical equation, (3.3): $\cdots$, A, B, C; $\cdots\triangledown\cdots$, D; $\cdots\bigcirc\cdots$, E. Numerical solution from (2.7) with no lift: – –, A, B, C; –▽–, D; –○–, E. Numerical solution from (2.7) with Auton's lift: ———, A, B, C; —▽——, D; —○—, E.

($St^2 \ll 1$) and neglecting the lift term in (2.7):

$$\frac{C_m(t)}{C_0} = \exp\left\{\frac{2\tau_b}{\nu}\left(\omega_0 \frac{k_x k_z}{k^3}\right)^2 [1 - \exp(-2\nu k^2 t)]\right\}. \tag{3.3}$$

In figure 6 our numerical solution for $C_m(t)/C_0$ is given, together with, for comparison, curves corresponding to (3.3) for Stokes numbers 0.5, 0.25 and 0.1 (cases E, A and D, respectively). As the Stokes number decreases, the accuracy of the analytical solution (3.3) improves as expected, resulting in better agreement with our numerical solution. Figure 6 also shows that the growth rate of $C_m(t)$ increases with Stokes number; we increase the Stokes number by augmenting the bubble response time; τ_b, via d_b in (2.9). Increasing τ_b reduces the radially outward drag force in (2.7) and thus increases the inward bubble acceleration toward the vortex centre, since $\mathrm{D}U_i/\mathrm{D}t$ is not affected by the bubbles in this one-way coupling case.

3.3. *Bubble-laden Taylor–Green vortex with two-way coupling*

We now discuss the effects of bubbles on the dynamics of the Taylor–Green vortex. The numerical results presented in this section were obtained by solving the governing equations (2.4)–(2.7).

3.3.1. *Effects of microbubbles on the dynamics of vorticity*

Figure 7 gives the instantaneous x-profiles of the vorticity ($\omega \equiv \omega_y$) at the middle plane of the computational domain, $z = 0.5$ (figure 1), and at time $t = 0.2$ for case A with one-way and two-way coupling. The figure shows that the bubbles cause a reduction in the vorticity magnitude in the central region of the vortices (figure 1) and no significant change elsewhere. The maximum reduction in vorticity magnitude (34 % at $t = 0.2$) occurs at the centres of the vortices ($x_c = 0.0$, 0.5, 1.0 and $z_c = 0.5$). Figure 7 also shows that the lift expressions of Auton and of Saffman produce nearly

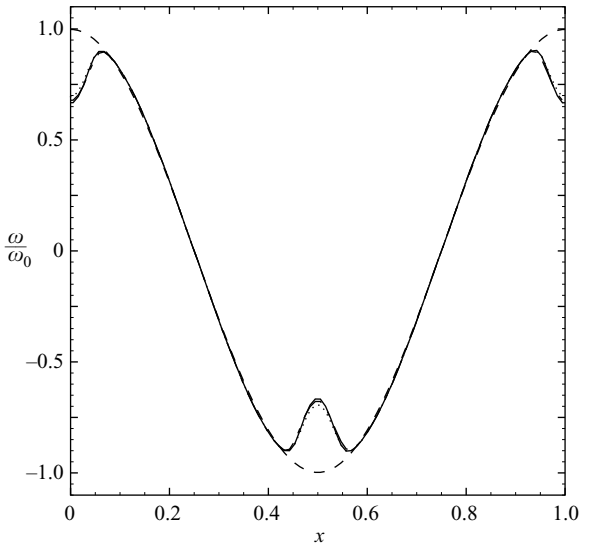

FIGURE 7. Instantaneous profiles of ω/ω_0 at $z=0.5$ and time $t=0.2$ for case A: one-way coupling (dashed line); two-way coupling with no lift (dotted line), Saffman's lift (small-and-large-dashed line) and Auton's lift (solid line) in (2.7).

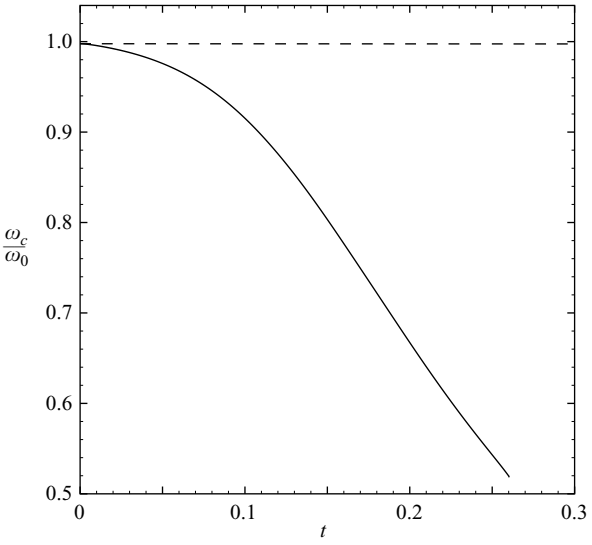

FIGURE 8. Temporal development of ω_c/ω_0 for case A: one-way coupling (dashed line); two-way coupling (solid curve).

identical results. Figure 8 gives the temporal developments of the vorticity magnitude $\omega_c(t)$ at the centre of the vortex,

$$\omega_c(t) = |\omega(x_c, z_c, t)|, \tag{3.4}$$

for case A with one-way and two-way coupling. In the one-way-coupling case, the vorticity $\omega_c(t)$ remains nearly invariant in time because the viscous diffusion of vorticity normalized by the initial maximum enstrophy is much smaller than 1 ($|\nu\nabla^2\omega|/\omega_0^2 \leqslant 8\times10^{-6}$). For the two-way-coupling case at time $t=0.2$, $\omega_c(t)$ is reduced

by about 34 % from its initial value (figures 7 and 8), and by about 46 % at time $t = 0.25$ (figure 8).

In order to explain how the bubbles reduce the vorticity in the central region of the vortices (figures 7 and 8), we examine the vorticity equation. The curl of the momentum equation of the carrier fluid (2.5) produces the following vorticity equation for a bubble-laden flow:

$$\underbrace{\partial_t \boldsymbol{\omega}}_{I} = \underbrace{\nu \nabla^2 \boldsymbol{\omega}}_{II} \underbrace{-(\boldsymbol{U}\cdot\nabla)\boldsymbol{\omega}}_{III} + \underbrace{(\boldsymbol{\omega}\cdot\nabla)\boldsymbol{U}}_{IV}$$
$$\underbrace{-\boldsymbol{\omega}(\nabla\cdot\boldsymbol{U})}_{V} \underbrace{-\frac{2\nu}{(1-C)^2}[\nabla(1-C)]\times[\nabla(1-C)\cdot\boldsymbol{S}]}_{VI} + \underbrace{\frac{2\nu}{(1-C)}\nabla\times[\nabla(1-C)\cdot\boldsymbol{S}]}_{VII}$$
$$+ \underbrace{\frac{1}{(1-C)^2}[\nabla(1-C)]\times\boldsymbol{f}}_{VIII} \underbrace{-\frac{1}{1-C}\nabla\times\boldsymbol{f}}_{IX}, \tag{3.5}$$

where $\boldsymbol{\omega}$ is the vorticity,

$$\boldsymbol{\omega} = \nabla\times\boldsymbol{U}, \tag{3.6}$$

and $\boldsymbol{S}$ is the strain-rate tensor,

$$\boldsymbol{S} \equiv \tfrac{1}{2}[\nabla\boldsymbol{U} + (\nabla\boldsymbol{U})^T]. \tag{3.7}$$

In (3.5), terms *I–IV* constitute the vorticity equation of an incompressible single-phase flow. Terms *V–IX* are due to the presence of the bubbles. In the following we describe the physical meaning of the terms on the right-hand side of (3.5).

(i) Terms *V*, *III* and *IV* originate from the nonlinear advection term in (2.5):

Term V represents the sink (source) of vorticity due to positive (negative) fluid-velocity divergence, i.e. expansion (compression) of the carrier fluid. This term vanishes for an incompressible single-phase flow. In a microbubble-laden flow, the carrier-fluid velocity may locally have non-zero divergence since the continuity equation (2.4) can be written as

$$\nabla\cdot\boldsymbol{U} = \frac{1}{1-C}[\partial_t C + \boldsymbol{U}\cdot\nabla C] = \frac{1}{1-C}\frac{\mathrm{D}C}{\mathrm{D}t}. \tag{3.8}$$

In the regions of the flow field where $\mathrm{D}C/\mathrm{D}t$ is positive (negative) due to bubble accumulation (dispersal), the carrier-fluid velocity field has positive (negative) divergence. Consequently, term *V* reduces (increases) the magnitude of the local vorticity in the flow regions where bubble accumulate (disperse).

Term III represents the advection of vorticity by the carrier-fluid velocity. This term vanishes in the single-phase two-dimensional TGV since the velocity vector and the gradient of the only vorticity component, ω_2, are perpendicular to each other at each point in the flow field.

Term IV represents the tilting and stretching of vorticity lines; it is

$$(\boldsymbol{\omega}\cdot\nabla)\boldsymbol{u} = [\omega_k\,\partial_k u_i]\,\boldsymbol{e}_i, \tag{3.9}$$

where $\boldsymbol{e}_i$ is the unit vector in the i-direction. This term contributes either to the conversion of ω_k to ω_i for $k \neq i$ or to the change in vorticity intensity caused by the stretching or contraction of vorticity lines for $k = i$. For our two-dimensional TGV, term *IV* equals zero.

(ii) The viscous terms *II*, *VI* and *VII* have the following meanings:

Term II represents the viscous diffusion of vorticity.

Case	*I*	*II*	*III*	*IV*	*V*
A(one-way)	7.9×10^{-6}	7.9×10^{-6}	0	0	0
A(two-way)	2.70×10^{-2}	5.8×10^{-5}	6.9×10^{-3}	0	2.65×10^{-2}
Case	*IV*	*VII*	*VIII*	*IX*	
A(one-way)	0	0	0	0	
A(two-way)	8.3×10^{-7}	6.3×10^{-6}	6.5×10^{-4}	2.1×10^{-3}	

TABLE 3. Maximum magnitude of terms *I*–*IX* of (3.5) normalized by ω_0^2 at time $t = 0.2$ in case A with one-way and two-way coupling.

Terms VI and *VII* are due to the interaction of the bubble-concentration gradient with the strain-rate tensor.

(iii) Terms *VIII* and *IX* are due to the two-way coupling force $\boldsymbol{f}$ between the bubbles and the fluid.

Term VIII is the cross-product of the bubble-concentration gradient and $\boldsymbol{f}$.

Term IX is the curl of $\boldsymbol{f}$. The coupling force enhances or reduces the magnitude of the vorticity depending on the alignment of $\boldsymbol{\omega}$ and curl $\boldsymbol{f}$. For example, in particle-laden isotropic turbulence with the particle Stokes number larger than 1, $\boldsymbol{\nabla} \times \boldsymbol{f}$ enhances the decay rate of the vorticity because of the fluid–particle drag interaction (see figure 17 of Ferrante & Elghobashi 2003).

Table 3 gives the computed maximum magnitude of each term of the vorticity equation (3.5) normalized by ω_0^2 at $t = 0.2$ in case A with one-way and two-way coupling. In case A with one-way coupling, only terms *I* and *II* of (3.5) are non-zero (they are $O(10^{-6})$) since (3.5) reduces to the vorticity equation of a single-phase TGV,

$$\partial_t \omega = \nu \nabla^2 \omega. \tag{3.10}$$

In case A with two-way coupling, in contrast, the maximum magnitude of the time rate of change of vorticity, term *I*, is approximately equal to term *V*, the sink or source of vorticity due to the divergence of the fluid velocity (both terms are $O(10^{-2})$), whereas all the other terms on the right-hand side of (3.5) are at least an order of magnitude smaller. Furthermore, the instantaneous contours of terms *I*–*IX* (not shown here) in the (x, z)-plane indicate that term *I* is approximately equal to term *V* throughout the computational domain:

$$\partial_t \omega \simeq -\omega (\boldsymbol{\nabla} \cdot \boldsymbol{U}). \tag{3.11}$$

Thus, it can be stated that in a bubble-laden TGV the local instantaneous magnitude of vorticity decreases when the local $\boldsymbol{\nabla} \cdot \boldsymbol{U}$ is positive and increases when it is negative. Figure 9 displays the instantaneous contours of $\boldsymbol{\nabla} \cdot \boldsymbol{U}$ normalized by ω_0 in case A with two-way coupling at $t = 0.2$; $\boldsymbol{\nabla} \cdot \boldsymbol{U}$ is positive (grey scale) in the circular zones (radius $\simeq 0.05$) located at the centres of the vortices (x_c and z_c), but is negative in the ring-shaped but slightly squared regions (dark blue) surrounded by four spiral arms (light blue), and is nearly zero elsewhere (lightest grey). The maximum value of $\boldsymbol{\nabla} \cdot \boldsymbol{U}$, which occurs at the centre of the vortices, is positive and about eight times larger than the magnitude of its negative peak ($0.039\,\omega_0$ versus $-0.005\,\omega_0$). Consequently, in the regions of positive $\boldsymbol{\nabla} \cdot \boldsymbol{U}$ the decay rate of the vorticity is larger than that in the case of one-way coupling (figures 7, 8 and 10). In the regions of small negative $\boldsymbol{\nabla} \cdot \boldsymbol{U}$, term *II* results in a small increase in the magnitude of vorticity at $t = 0.2$, as shown in figure 10 (at $x = 0.44$ and 0.56).

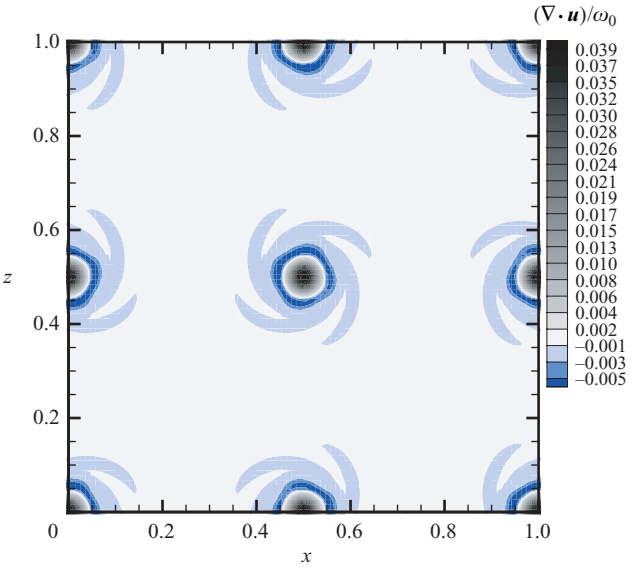

FIGURE 9. Instantaneous contours of $\nabla\cdot\boldsymbol{U}/\omega_0$ at time $t=0.2$ for case A with two-way coupling.

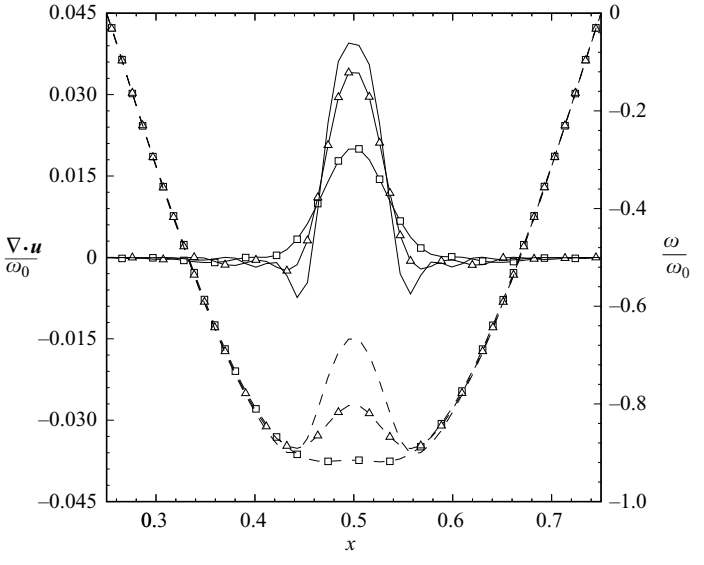

FIGURE 10. Instantaneous x-profiles of $\nabla\cdot\boldsymbol{U}$ (solid lines) and ω/ω_0 (dashed lines) at $z=0.5$ and times $t=0.1$ (squares), 0.15 (triangles) and 0.2 (no symbols) for case A with two-way coupling.

It is clear from the above discussion that $\nabla\cdot\boldsymbol{U}$ is responsible for modulating of the vorticity field of the bubble-laden TGV. We now discuss how the bubbles produce a non-zero $\nabla\cdot\boldsymbol{U}$. The fluid continuity equation (3.8) shows that the $\nabla\cdot\boldsymbol{U}$ is proportional to the sum of $\partial_t C$ and $\boldsymbol{U}\cdot\nabla C$. Figure 11 shows the instantaneous x-profiles at $t=0.2$ and $z=0.5$ of these three quantities. It is clear that $\partial_t C$ is the main contributor to $\nabla\cdot\boldsymbol{U}$ in the vortex core ($0.46\leqslant x\leqslant 0.54$) whereas both $\boldsymbol{U}\cdot\nabla C$

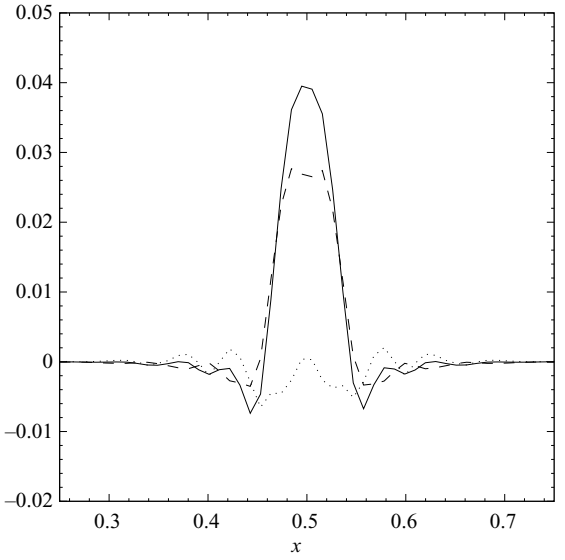

FIGURE 11. Instantaneous profiles of $\nabla \cdot \boldsymbol{U}$ (solid line), $\partial_t C$ (dashed line) and $\boldsymbol{U} \cdot \nabla C$ (dotted line) at $z = 0.5$ and time $t = 0.2$ for case A with two-way coupling.

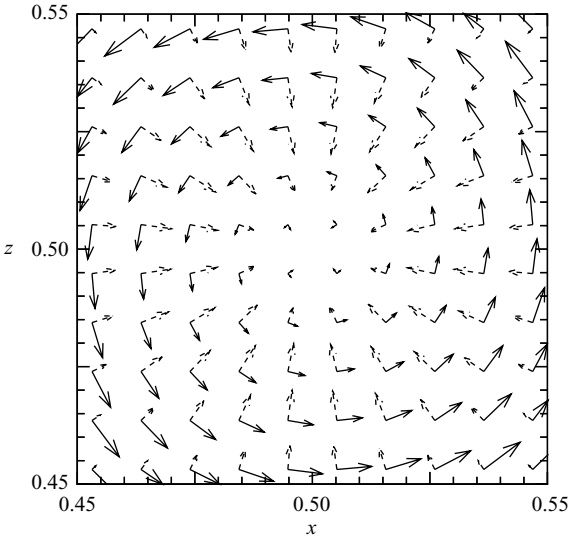

FIGURE 12. Instantaneous $\boldsymbol{U}$ vectors (solid arrows) and ∇C vectors (dashed arrows) at time $t = 0.2$ for case A with two-way coupling.

and $\partial_t C$ have comparable effects outside the core. Figure 12 shows that the $\boldsymbol{U}$ and ∇C vectors are nearly perpendicular throughout the flow field; thus their dot product is negligible compared with $\partial_t C$. Since bubbles move along spiral trajectories (figure 3) towards the vortex centre, C increases in the vortex core ($\partial_t C > 0$) and decreases in the surrounding ring ($\partial_t C < 0$), as shown in figure 11. Furthermore, the instantaneous contours of $\partial_t C$ at time $t = 0.2$ (not shown here) resemble the contours of $\nabla \cdot \boldsymbol{U}$ (figure 9).

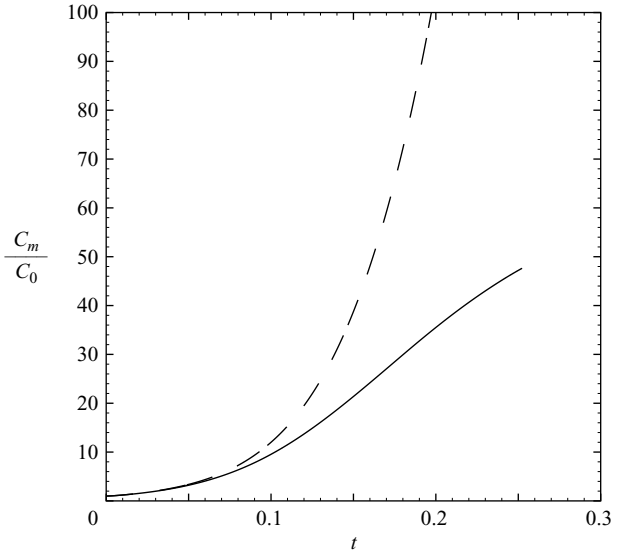

FIGURE 13. Temporal development of C_m/C_0 for case A: one-way coupling (dashed line); two-way coupling (solid line).

It is of interest to comment on the experimental results of Sridhar & Katz (1999, hereafter referred to as SK) using the vorticity equation (3.5). In their experiment, five bubbles with $484\,\mu\text{m} \leqslant d_b \leqslant 1100\,\mu\text{m}$ were injected into a vortex ring. SK reported that the buoyancy and pressure-gradient coupling forces (f_i in (2.8)), imparted to the fluid by the entrained bubbles, distort the vortex core and increase the maximum vorticity and circulation. It should be noted that the local two-dimensional concentration C_{2D} of the bubbles in the vortex core of SK's experiment is about 10^{-3}, in contrast with our present study where the initial $C_{2D} = 0.16$ and the acceleration due to gravity is set to zero. Although the five bubbles in SK's vortex ring do not constitute a continuum it can be shown that in SK's experiment the magnitude of $\nabla \cdot \boldsymbol{U}$ (see (3.8)) is much smaller than that of $(\nabla \times \boldsymbol{f})/(1 - C)$ (i.e. term $V \ll$ term IX in the vorticity equation (3.5)). Thus, whereas the concentration of a large number (10^5) of microbubbles in our zero-gravity symmetrical TGV causes a significant reduction in vorticity, the much smaller (by two orders of magnitude) concentration of very few (five) larger buoyant bubbles increases the vorticity in the asymmetric vortex ring of SK.

3.3.2. *Two-way coupling effects on bubble concentration at the centre of the vortex*

We now discuss the two-way coupling effects on the bubble concentration at the centre of the vortex. The reduction in vorticity in the two-way coupling case, figure 7, corresponds to a reduction in the magnitude of $\mathrm{D}\boldsymbol{U}/\mathrm{D}t$ (the first term on the right-hand side of (2.7)), compared with the one-way coupling case, in the neighbourhood of the vortex centre ($x = 0.0,\ 0.5,\ 1.0$) (not shown here). Consequently, in the two-way coupling case the bubble acceleration toward the vortex centre is reduced and thus the maximum concentration of bubbles $C_m(t)$ is smaller than that for one-way coupling (figure 13). The difference between the values of $C_m(t)$ in the two cases is negligible at early times, $t \leqslant 0.05 = 20\tau_b$, and becomes significant ($>10\%$) for $t \geqslant 0.09$, when the vorticity $\omega_c(t)$ in the two-way coupling case is about 7 % smaller than that in one-way coupling (figure 8). Figures 5 and 14 show the instantaneous concentration field in

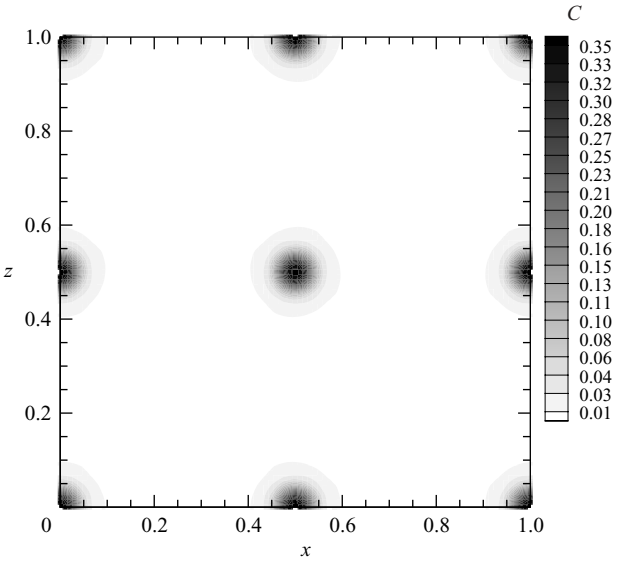

FIGURE 14. Instantaneous contours of the bubble concentration C at time $t = 0.2$ for case A (with two-way coupling).

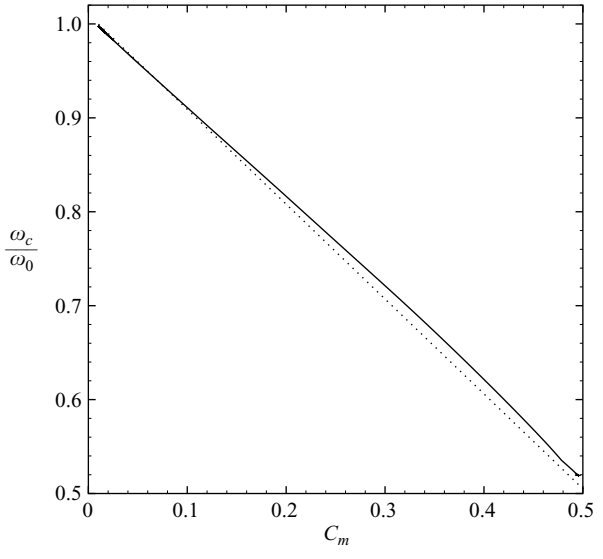

FIGURE 15. The ratio ω_c/ω_0 vs. C_m for case A with two-way coupling: approximate analytical equation (3.26) (dotted line); numerical solution (solid line).

the (x, z)-plane at time $t = 0.2$ in case A for one-way and for two-way coupling, respectively. In both cases the isocontours of C are of nearly circular shape, but the maximum concentration is reduced from 1.0 in one-way coupling to 0.35 in two-way coupling. We expect that if the hydrodynamic interactions between the bubbles are accounted for then the repulsion forces will keep the bubbles apart and thus the maximum concentration in the vortex core will be smaller than that presented here.

We note that at time $t = 0.2$, when $C_m = 0.35$ (figures 13 and 14), ω_c is reduced by 34 % from its initial value (figure 8). Figure 15 shows that the numerical solution for

ω_c (solid line) is nearly a decreasing linear function of C_m. The numerical ω_c agrees well with the approximate analytical solution (3.26) of the vorticity equation, which will be discussed in the next section.

3.3.3. *Analytical solution for the vorticity and bubble concentration at the vortex centre*

The temporal development of the bubble concentration, $C_m(t)$, and the fluid vorticity, $\omega_c(t)$, at the centre of the Taylor–Green vortex can be obtained analytically provided that the Stokes number, $St = \tau_b \omega_0$, is smaller than 1, and such that

$$St^2 \ll 1, \tag{3.12}$$

and that the viscous effects are small compared with the two-way coupling effects, i.e. the non-dimensional viscosity divided by C_0 is small,

$$\nu / C_0 \ll 1, \tag{3.13}$$

which can also be expressed as

$$Re\, C_0 \gg 1, \tag{3.14}$$

where Re is the Reynolds number. Assuming that (3.12) and (3.14) are satisfied, we can write the equations of vorticity and bubble-phase continuity in approximate forms which are valid in the vicinity of the vortex centre. These coupled equations, derived below, form a system of two first-order ordinary differential equations in the unknowns $C_m(t)$ and $\omega_c(t)$. The analytical solution of these equations is then evaluated and compared with the numerical solution.

Under the assumption (3.12), and neglecting the lift term in the momentum equation for the bubble phase, (2.7), an approximate solution of (2.7) can be written in the form (Maxey 1987*a*; Druzhinin & Elghobashi 1998)

$$\boldsymbol{V} = \boldsymbol{U} + 2\tau_b \frac{\mathrm{D}\boldsymbol{U}}{\mathrm{D}t} + O(St^2). \tag{3.15}$$

Substituting (3.15) into the bubble-phase continuity equation (2.6) we obtain

$$\partial_t C + \nabla\cdot(C\boldsymbol{U}) = -2\tau_b \nabla\cdot\left(C\frac{\mathrm{D}\boldsymbol{U}}{\mathrm{D}t}\right). \tag{3.16}$$

Equation (2.4) can also be rewritten as

$$\nabla\cdot\boldsymbol{U} = \frac{1}{1-C}\frac{\mathrm{D}C}{\mathrm{D}t}. \tag{3.17}$$

The second term on the left-hand side of (3.16) can be written via (3.17) as

$$\nabla\cdot(C\boldsymbol{U}) = \frac{C}{1-C}\frac{\mathrm{D}C}{\mathrm{D}t} + \boldsymbol{U}\cdot\nabla C; \tag{3.18}$$

thus (3.16) becomes

$$\frac{1}{1-C}\frac{\mathrm{D}C}{\mathrm{D}t} = -2\tau_b \nabla\cdot\left(C\frac{\mathrm{D}\boldsymbol{U}}{\mathrm{D}t}\right). \tag{3.19}$$

In the vicinity of the vortex centre (e.g. $x_c = 0$, $z_c = 0$), the fluid-velocity field can be approximated by that of a 'solid' rotation whose intensity is $\omega_c(t) = |\omega(x_c, z_c, t)|$, since the rotational part of the fluid velocity is significantly larger than $\nabla\cdot\boldsymbol{U}$, as shown in

figure 9. Thus the fluid-velocity components (see (3.1)) in the x- and z-directions are

$$U_1^c \simeq -\omega_c(t)\frac{k_z^2}{k^2}z,$$
$$U_3^c \simeq \omega_c(t)\frac{k_x^2}{k^2}x, \tag{3.20}$$

for $|x| \ll 1$ and $|z| \ll 1$, where k_x and k_z are the wavenumbers in the x- and z-directions and $k^2 = k_x^2 + k_z^2$.
Substituting (3.20) into (3.19) we obtain

$$\frac{1}{1-C}\frac{\mathrm{D}C}{\mathrm{D}t} \simeq \frac{4k_x^2k_z^2}{k^4}\,\tau_b\,\omega_c^2\,C - 2\tau_b\frac{\mathrm{D}\boldsymbol{U}}{\mathrm{D}t}\cdot\nabla C. \tag{3.21}$$

At the vortex centre, the concentration of bubbles is a maximum, $C(x_c, z_c, t) = C_m(t)$; thus its gradient is zero and (3.21) becomes

$$\frac{C_m'}{C_m(1-C_m)} \simeq \frac{4k_x^2k_z^2}{k^4}\,\tau_b\,\omega_c^2, \tag{3.22}$$

where the prime denotes a first-order derivative with respect to time. The dynamics of $\omega_c(t)$ is described by the vorticity equation (3.6), which can be approximated via (3.13) as

$$\omega_c' \simeq -\omega_c(\nabla\cdot\boldsymbol{U})_c. \tag{3.23}$$

At the vortex centre (3.17) becomes

$$(\nabla\cdot\boldsymbol{U})_c = \frac{C_m'}{1-C_m}. \tag{3.24}$$

Substitution of (3.24) into (3.23) gives

$$\frac{\omega_c'}{\omega_c} \simeq -\frac{C_m'}{1-C_m}. \tag{3.25}$$

For an initial vorticity ω_0 and bubble concentration C_0, the time integration of (3.25) gives ω_c as function of C_m:

$$\frac{\omega_c}{\omega_0} = \frac{1-C_m}{1-C_0}. \tag{3.26}$$

Substituting (3.26) into (3.22) and integrating the resulting equation over time gives the temporal development of C_m as:

$$\ln\left(\frac{C_m}{1-C_m}\right) + \frac{1}{1-C_m} + \frac{1}{2(1-C_m)^2}$$
$$= \ln\left(\frac{C_0}{1-C_0}\right) + \frac{1}{1-C_0} + \frac{1}{2(1-C_0)^2} + \frac{4k_x^2k_z^2}{k^4}\,\frac{St\,\omega_0}{(1-C_0)^2}\,t. \tag{3.27}$$

The approximate analytical solution for the divergence of fluid velocity, $(\nabla\cdot\boldsymbol{U})_c$, at the vortex centre is obtained via substitution of (3.22) and (3.26) into (3.24) as

$$(\nabla\cdot\boldsymbol{U})_c = \frac{4k_x^2k_z^2}{k^4}\,St\,\omega_0\,C_m\left(\frac{1-C_m}{1-C_0}\right)^2. \tag{3.28}$$

Figure 16 shows the temporal development of C_m for both the analytical (3.27) and numerical solutions neglecting the lift term in (2.7). The analytical and numerical solutions for case D ($St = 0.1$ and $C_0 = 0.01$) are nearly identical. As the Stokes number increases, from 0.1 to 0.25 to 0.5 for cases D, A and E, respectively, the assumption (3.12) becomes less valid; thus the deviation of the approximate analytical

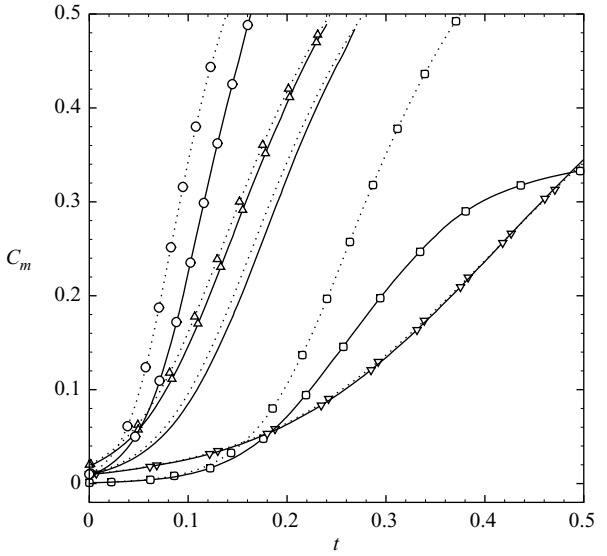

FIGURE 16. Temporal development of C_m for cases A–E with two-way coupling. Approximate analytical equation, (3.27): ···, A; ···□···, B; ···△···, C; ···▽···, D; ···○···, E. Numerical solution (no lift): ——, A; —□—, B; —△—, C; —▽—, D; —○—, E.

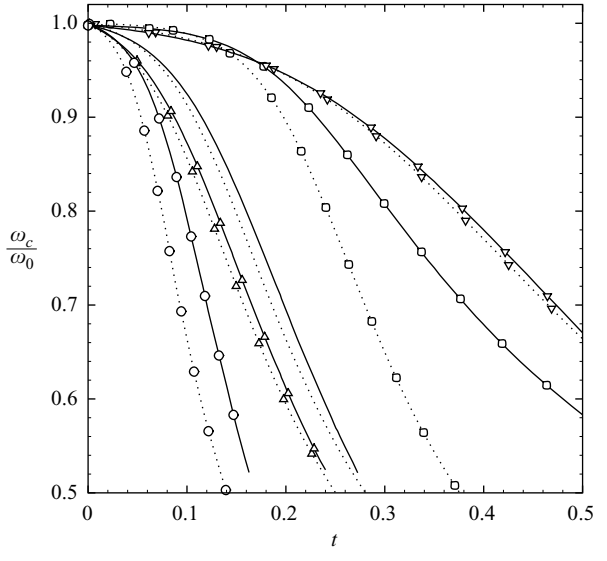

FIGURE 17. Temporal development of ω_c/ω_0 for cases A–E with two-way coupling. Approximate analytical equations (3.26) and (3.27): ·····, A; ·····□·····, B; ·····△·····, C; ·····▽·····, D; ·····○·····, E. Numerical solution with no lift in (2.7): ——, A; —□—, B; —△—, C; —▽—, D; —○—, E.

solution $C_m(t)$ from the more accurate numerical solution increases correspondingly. Raising the initial concentration C_0 from 0.001 (case B) to 0.02 (case C) increases the accuracy of the analytical solution and enhances its agreement with the numerical solution, since (ν/C_0) becomes smaller and (3.13) is satisfied. Similar comments can be made about the accuracy of the analytical solutions of $\omega_c(t)$ and $(\nabla \cdot \boldsymbol{U})_c(t)$ shown in figures 17 and 18 respectively.

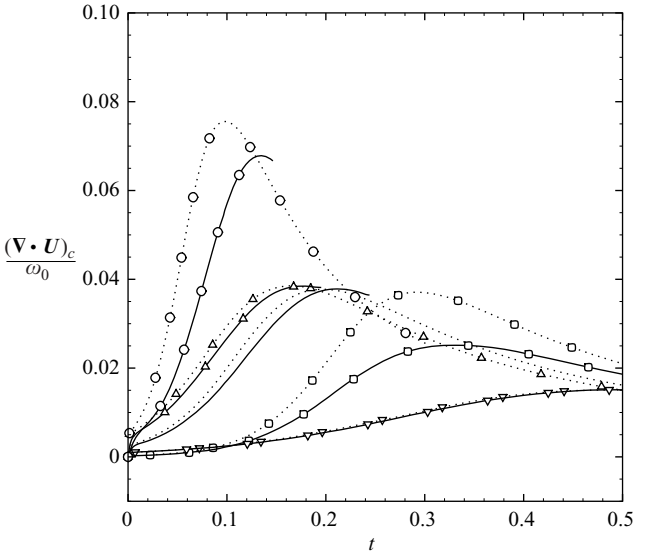

FIGURE 18. Temporal development of $(\nabla \cdot \boldsymbol{U})_c/\omega_0$ for cases A–E with two-way coupling: approximate analytical equations (3.28) and (3.27) (dotted lines); numerical solution with no lift in (2.7) (solid lines). Symbols as in figure 17.

We now explain the effects of C_0 and St on the temporal development of C_m, ω_c and $(\nabla \cdot \boldsymbol{U})_c$. As C_0 increases from 0.001 to 0.01 to 0.02 (cases B, A and C), while St is kept constant, the number of bubbles moving towards the vortex centre increases and thus both C_m and its growth rate C_m' increase (figure 16). Similarly, as St increases from 0.1 to 0.25 to 0.5 (cases D, A and E), while C_0 is kept constant, both C_m and its growth rate C_m' increase (figure 16) because the inward bubble acceleration toward the vortex centre increases, as explained in § 3.2 for the one-way coupling case. Consequently, both $(\nabla \cdot \boldsymbol{U})_c$ and the decay rate of ω_c increase with an increase in either C_0 or St while the other parameter is kept constant (figures 18 and 17) because both C_m and C_m' increase in (3.24) and (3.25).

We now compare the results of (3.26) with the numerical solution in figure 15: the maximum difference between the numerical and analytical solutions of $\omega_c(C_m)$ is less than 3 %. Equation (3.26) shows that ω_c/ω_0 is a linear function of C_m whose slope is equal to $-(1-C_0)^{-1} \simeq -1$ and whose intercept is equal to $(1-C_0)^{-1} \simeq 1$; thus (3.26) can be approximated as:

$$1 - \frac{\omega_c}{\omega_0} \simeq C_m. \tag{3.29}$$

This equation and figure 15 indicate that the reduction in the magnitude of vorticity at the vortex centre from its initial value is approximately equal to the bubble volume fraction at the centre.

3.3.4. *Effects of microbubbles on the temporal development of the mean enstrophy*

We discussed in § 3.3.1 the effects of bubbles on the vorticity dynamics in a TGV. We now investigate how the bubbles modify the temporal development of the instantaneous mean enstrophy. The mean enstrophy (spatially averaged over the

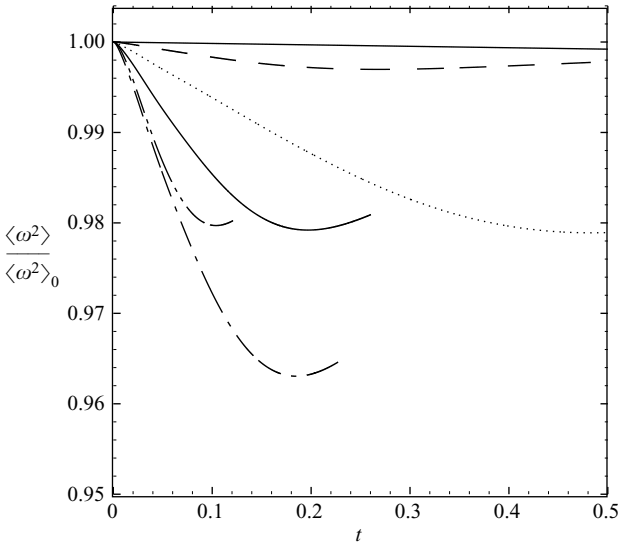

FIGURE 19. Temporal development of $\langle\omega^2\rangle/\langle\omega^2\rangle_0$ in the single-phase flow (nearly horizontal solid line) and for cases A–E with two-way coupling: solid curve, A; dashed curve, B; dashed-and-dotted curve, C; dotted curve, D; dashed-and-double-dotted curve, E.

Case	C_0	St	t_{min}	$1-\langle\omega^2\rangle(t_{min})/\langle\omega^2\rangle_0$
A	0.01	0.25	0.197	0.0208
B	0.001	0.25	0.295	0.0030
C	0.02	0.25	0.184	0.0370
D	0.01	0.1	0.483	0.0211
E	0.01	0.5	0.104	0.0203

TABLE 4. Maximum reduction in $\langle\omega^2\rangle(t)/\langle\omega^2\rangle_0$ and the time t_{min} at which this reduction occurs, for cases A–E with two-way coupling.

(x, z)-plane) is computed as

$$\langle\omega^2\rangle(t) = \frac{1}{N^2}\sum_{i=1}^{N}\sum_{k=1}^{N}\omega^2(x_i, x_k, t), \tag{3.30}$$

where N is the number of grid points in the x- and z-spatial directions, $x_i = i\,\Delta x$ and $x_k = k\Delta x$. Figure 19 shows the temporal development of $\langle\omega^2\rangle$ normalized by its initial value, $\langle\omega^2\rangle_0$, for cases A–E with two-way coupling and the single-phase flow (SPF). In the SPF the mean enstrophy monotonically decays in time because of viscous diffusion:

$$\partial_t\langle\omega^2\rangle = \nu\langle\nabla^2\omega^2\rangle. \tag{3.31}$$

Figure 19 shows that, for $t > 0$ in cases A–E with two-way coupling, the enstrophy $\langle\omega^2\rangle/\langle\omega^2\rangle_0$ is smaller than that for the single-phase TGV and that the initial decay rate of $\langle\omega^2\rangle$ in these five cases is larger than that for SPF. The figure also shows that $\langle\omega^2\rangle$ first decays, reaches a minimum and then increases. The minimum of $\langle\omega^2\rangle$ occurs at a time, t_{min}, which increases as either St or C_0 is reduced (table 4). Table 4 also shows that the maximum reduction in $\langle\omega^2\rangle$ from its initial value increases with

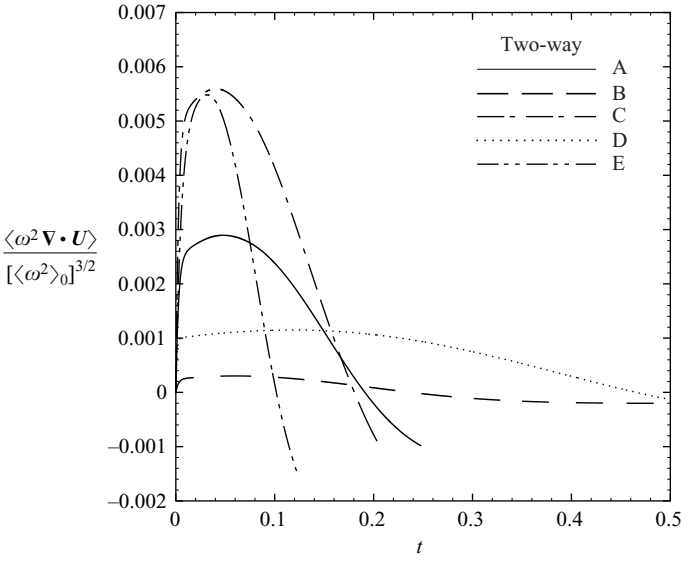

FIGURE 20. Temporal development of $\langle\omega^2\nabla\cdot\boldsymbol{U}\rangle/[\langle\omega^2\rangle_0]^{3/2}$ in cases A–E with two-way coupling. Key as in figure 19.

C_0 for fixed St (cases B, A and C) but remains nearly constant with increasing St for fixed C_0 (cases D, A and E).

The above observations about the temporal development of the spatial-mean enstrophy in a bubble-laden TGV (figure 19) can be explained by the spatial-mean-enstrophy equation, which is obtained from the approximate vorticity equation (3.11) as

$$\partial_t\,\omega^2 \simeq -2\,\omega^2\,\nabla\cdot\boldsymbol{U}. \tag{3.32}$$

Averaging (3.32) over the (x, z)-plane we obtain the spatial-mean-enstrophy equation:

$$\partial_t\langle\omega^2\rangle \simeq -2\langle\omega^2\,\nabla\cdot\boldsymbol{U}\rangle. \tag{3.33}$$

This equation indicates that the mean enstrophy decays if the spatial correlation of ω^2 and $\nabla\cdot\boldsymbol{U}$ is positive, and vice versa. Bubbles reduce the mean enstrophy in the TGV initially ($0 < t < t_{min}$, figure 19) because their accumulation in the high-enstrophy core regions produces a positive correlation between ω^2 and $\nabla\cdot\boldsymbol{U}$. Figure 20 shows that the correlation, which is $\langle\omega^2\,\nabla\cdot\boldsymbol{U}\rangle = 0$ at $t = 0$, increases with time, reaches a maximum, decreases to zero at $t \simeq t_{min}$ (i.e. when $\langle\omega^2\rangle$ has a minimum) and then becomes negative, since a negative, $\nabla\cdot\boldsymbol{U}$ is correlated with high enstrophy in the ring outside the core region (figure 10) whereas a positive $\nabla\cdot\boldsymbol{U}$ is correlated with the reduced enstrophy in the core region.

We now explain how $\langle\omega^2\rangle(t_{min})$ and t_{min} depend on C_0 and St (figure 19 and table 4) as mentioned earlier in this section. Since $\partial_t C$ is larger than $\boldsymbol{U}\cdot\nabla C$ in the vortex core, as explained in § 3.3.1, the continuity equation (3.8) can be written as

$$\nabla\cdot\boldsymbol{U} \simeq \frac{\partial_t C}{1-C}. \tag{3.34}$$

Substituting (3.34) into (3.32) we have

$$\partial_t\,\omega^2 \simeq -2\,\omega^2\left(\frac{\partial_t C}{1-C}\right). \tag{3.35}$$

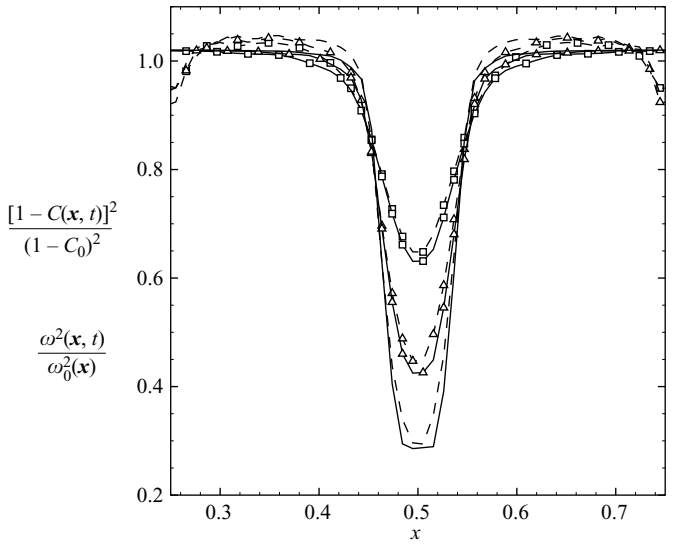

FIGURE 21. Instantaneous profiles of $[1-C(\boldsymbol{x},t)]^2/(1-C_0)^2$ (solid lines) and $\omega^2(\boldsymbol{x},t)/\omega_0^2(\boldsymbol{x})$ (dashed lines) at $z=0.5$ and times $t=0.15$ (squares), 0.2 (triangles) and 0.25 (no symbols) for case A with two-way coupling.

Integrating (3.35) in time we obtain

$$\frac{\omega^2(\boldsymbol{x},t)}{\omega_0^2(\boldsymbol{x})} \simeq \frac{[1-C(\boldsymbol{x},t)]^2}{(1-C_0)^2}, \tag{3.36}$$

where $\omega_0^2(\boldsymbol{x})$ is the local enstrophy at time $t=0$. Figure 21 shows the temporal development of both sides of (3.36) for case A. The figure displays the validity of (3.36), i.e. the proportionality of the decay in $\omega^2(\boldsymbol{x},t)$ and the increase in $C^2(\boldsymbol{x},t)$, especially in the core region. The discrepancy between the right-hand side and the left-hand side in the outer ring ($0.56 \leqslant x \leqslant 0.7$) and ($0.3 \leqslant x \leqslant 0.42$) is due to neglecting $\boldsymbol{U}\cdot\nabla C$ (see the remarks before (3.34)), which is of the same order of $\partial_t C$ in the ring as mentioned in § 3.3.3 (figure 11). As C_0 increases (cases B, A and C), while St is kept constant, the number of bubbles moving towards the vortex core increases; thus both C and its growth rate, $\partial_t C$, increase in the vortex core. Consequently, $\nabla\cdot\boldsymbol{U}$ increases via (3.34) and ω^2 decreases via (3.36) in the core, where $(1-C)^2 < (1-C_0)^2$. The net result is that, as C_0 increases, the correlation $\langle\omega^2\,\nabla\cdot\boldsymbol{U}\rangle$ grows and decays in a shorter time (figure 20); thus t_{min} decreases with C_0 (table 4).

In § 3.3.3 we showed that as St increases, while C_0 is kept constant (cases D, A and E), the growth rate of $C_m(t)$ and the decay rate of $\omega_c(t)$ increase, i.e. the accumulation of bubbles in the vortex centre and the consequent vorticity reduction occur in a shorter time. Thus, as St increases, the temporal growth and decay rates of $\langle\omega^2\nabla\cdot\boldsymbol{U}\rangle$ increase (figure 20) and the time t_{min} decreases (table 4). Furthermore, increasing St while keeping C_0 constant increases the growth rate of C in the vortex core. Thus the initial decay rate of $\langle\omega^2\rangle$ increases with St, whereas the value of $\langle\omega^2\rangle(t_{min})$ remains approximately the same (figure 19 and table 4).

4. Concluding remarks

The objective of the study that we have described in the previous sections is to examine the effects of microbubbles on the vorticity dynamics in a two-dimensional

Taylor–Green vortex flow (TGV). We have developed, for that purpose, a novel predictor–corrector numerical method to solve the two-fluid (or Eulerian–Eulerian) equations for bubble-laden flows with average bubble concentration $C_0 \sim 10^{-2}$. The main results of our study are as follows.

(i) Bubbles enhance the decay rate of the magnitude of the vorticity at the centre of the vortex compared with that of the single-phase flow. For example, bubbles with Stokes number equal to 0.25 and volume fraction 1 % reduce the magnitude of the vorticity at the centre of the vortex, after 20 turnover times of the initial vortex, by 34 % as compared to that of the single-phase flow. Analysis of the vorticity equation shows that the local positive velocity divergence of the fluid velocity, $\nabla \cdot \boldsymbol{U}$, created in the vortex core by bubble clustering, is responsible for the vorticity decay.

(ii) At the centre of the vortex, the vorticity $\omega_c(t)$, decreases nearly linearly with the bubble concentration $C_m(t)$. Similarly, the enstrophy in the core of the vortex, $\omega^2(t)$, decays linearly with $C^2(t)$.

(iii) Analysis of the approximate mean-enstrophy equation shows that bubble accumulation in the high-enstrophy core regions produces a positive correlation between ω^2 and $\nabla \cdot \boldsymbol{U}$, which enhances the decay rate of the mean enstrophy.

This work was supported by ONR Grant No. N00014-05-1-0059, and the computations were performed on the CRAY-T3E located at the US Army High Performing Computing Research centre (AHPCRC), Minnesota.

Appendix A. Numerical-method details

In this section we describe our numerical method for solving the governing equations (2.4)–(2.7) of a bubble-laden flow with two-way coupling, and in the next section we describe the solution method for a flow with one-way coupling.

A.1. *Two-way coupling*

In order to solve (2.4)–(2.7) numerically, we rewrite the momentum equations (2.5) and (2.7) as follows. The left-hand side of (2.5) can be written via (2.4) as

$$\begin{aligned}\partial_t[(1-C)\,U_i] + \partial_j[(1-C)\,U_i\,U_j] &= (1-C)[\partial_t U_i + U_j \partial_j U_i] \\ &= (1-C)[\partial_t U_i + \partial_j(U_i U_j) - U_i \partial_j U_j]. \quad \text{(A 1)}\end{aligned}$$

On substitution of (A 1) into (2.5) and division throughout by $(1-C)$, the carrier-fluid momentum equation in conservative form, (2.5), takes the quasi-non-conservative form

$$\begin{aligned}\partial_t U_i = &-\partial_i P - \partial_j(U_i U_j) + U_i \partial_j U_j + \frac{\nu}{1-C}\,\partial_j[(1-C)\,(\partial_j U_i + \partial_i U_j)] \\ &- \frac{f_i}{1-C} + g_i. \quad \text{(A 2)}\end{aligned}$$

Similarly, the bubble-phase momentum equation (2.7) can be written as

$$\partial_t V_i = -\partial_j(V_i V_j) + V_i \partial_j V_j + 3\frac{\mathrm{D}U_i}{\mathrm{D}t} + \frac{1}{\tau_b}(U_i - V_i) + [(\boldsymbol{U}-\boldsymbol{V}) \times \boldsymbol{\omega}]_i. \quad \text{(A 3)}$$

We define RU_i, RC and RV_i as follows:

$$RU_i \equiv -\partial_j(U_i U_j) + U_i \partial_j U_j + \frac{\nu}{1-C}\,\partial_j[(1-C)\,(\partial_j U_i + \partial_i U_j)] - \frac{f_i}{1-C} + g_i, \quad \text{(A 4)}$$

$$RC \equiv -\partial_i(C V_i), \quad \text{(A 5)}$$

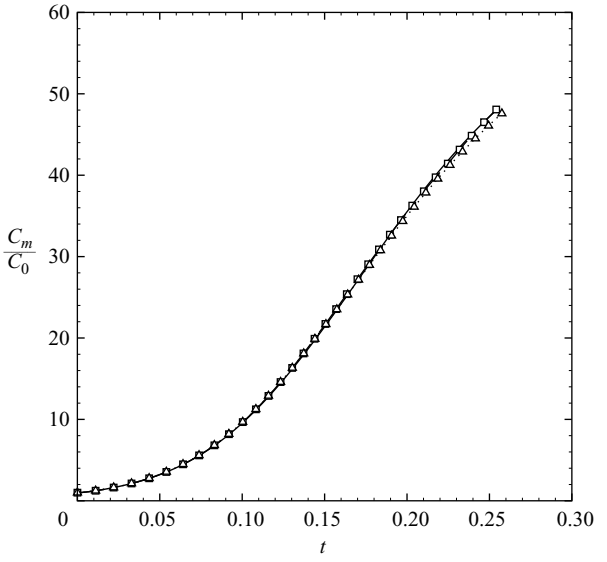

FIGURE 22. Temporal development of C_m/C_0 for case A with two-way coupling using three different computational meshes: $96 \times 2 \times 96$ (solid line), $128 \times 2 \times 128$ (dashed line with squares) and $256 \times 2 \times 256$ (dotted line with triangles).

$$RV_i \equiv -\partial_j(V_i V_j) + V_i \partial_j V_j + 3\frac{\mathrm{D}U_i}{\mathrm{D}t} + \frac{1}{\tau_b}(U_i - V_i) + [(\boldsymbol{U} - \boldsymbol{V}) \times \boldsymbol{\omega}]_i, \tag{A 6}$$

such that (A 2), (2.6) and (A 3) can be rewritten in compact form as

$$\partial_t U_i = -\partial_i P + RU_i, \tag{A 7}$$

$$\partial_t C = RC, \tag{A 8}$$

$$\partial_t V_i = RV_i. \tag{A 9}$$

Equations (2.4), (A 7), (A 8) and (A 9) are solved numerically using a newly developed predictor–corrector method, similar to that described by Najm, Wyckoff & Knio (1998) for simulating unsteady combustion in two dimensions. The main differences between the present method and that described by Najm *et al.* (1998) are given later in this section. Our predictor uses a second-order Adams–Bashforth time-integration scheme to time advance the velocities U_i and V_i and the scalar field C. Our corrector uses a second-order Crank–Nicolson time-integration scheme. In order to satisfy the continuity equation for the carrier fluid, (2.4), a Poisson equation for the pressure is solved in both the predictor and corrector steps, (A 16) and (A 25), and a pressure correction is applied to the velocity field U_i, (A 18) and (A 27). Although, the TGV flow studied here is two-dimensional, the numerical method uses a three-dimensional algorithm, where the flow is homogeneous in the y-direction. The three-dimensional computational domain contains two planes in the y-direction and a mesh of $96 \times 2 \times 96$ grid points in the x-, y- and z-directions respectively, with uniform grid spacing. Grid refinement tests are performed on $128 \times 2 \times 128$ and $256 \times 2 \times 256$ grids. Figure 22 shows that the three different grids produce nearly identical distributions of $C_m(t)/C_0$. The scalar fields P and C are computed at the cell centres, whereas the staggered velocity components are computed at the centres of the cell sides. The spatial derivatives in (A 4) and (A 6) for RU_i and RV_i are computed using second-order central finite differences. In order to ensure the positivity of the

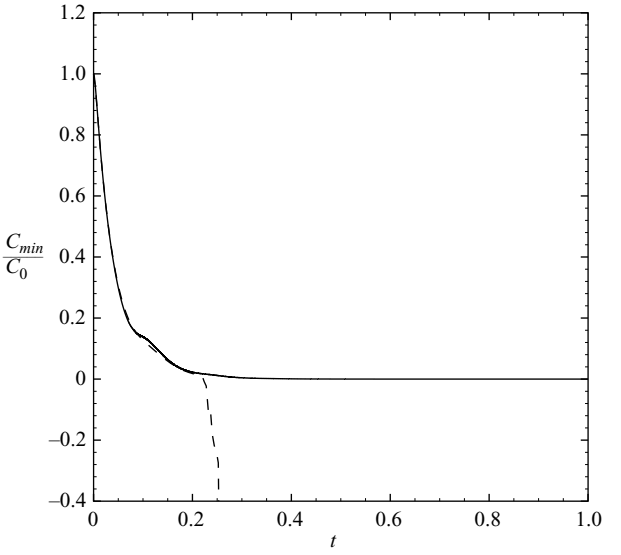

FIGURE 23. Temporal development of C_{min}/C_0 for case A with one-way coupling: central-difference scheme (CDS) to discretize RC in (A 5) (dashed line); MUSCL-TVD scheme to discretize RC in (A 5) (solid line).

scalar field C, we compute RC in (A 5) using a MUSCL-TVD (monotone upstream-centred scheme for conservation laws – total-variation-diminishing) scheme (Van Leer 1979; Hirsch 1990, pp. 552–553) with the 'Superbee' flux-limiter function developed by Roe (1985). Figure 23 shows that the minimum bubble-phase concentration C in case A (one-way coupling) becomes negative at time $t = 0.25$ when using the second-order central difference scheme, and stays positive in time when using the MUSCL-TVD scheme.

The main differences between the present numerical method and that described by Najm *et al.* (1998) are: (*a*) our algorithm is three-dimensional and theirs is two-dimensional; (*b*) we implement the MUSCL-TVD scheme to discretize RC (A 5) and so ensure the positivity of C; (*c*) we discretize the quasi-non-conservative form of the momentum equation (A 2) and (A 4) whereas they use the conservative form (see equations (2), (3), (12) and (13) from Najm *et al.* 1998); (*d*) we express the time derivative $\partial_t C$ in (A 17) and (A 26) below using the bubble-phase continuity equation (2.6), whereas they use second-order time discretization (see equation (15) from Najm *et al.* 1998). The stability of our numerical method has been considerably enhanced via (*c*) and (*d*).

Predictor The following seven steps, (*a*) to (*g*), constitute the predictor.

(*a*) The Lagrangian derivatives of the fluid-velocity components, $\mathrm{D}U_i^n/\mathrm{D}t$, which are required to compute the coupling force f_i^n from (2.8) and RV_i^n from (A 6), are evaluated as

$$\frac{\mathrm{D}U_i^n}{\mathrm{D}t} = \partial_t U_i^n + \partial_j\left(U_i^n U_j^n\right) - U_i^n \partial_j U_j^n, \tag{A 10}$$

where the superscripts indicate the time level, i.e. $U_i^n = U_i(\boldsymbol{x}, t^n)$, and

$$\partial_t U_i^n = \frac{U_i^n - U_i^{n-1}}{\Delta t}. \tag{A 11}$$

(*b*) The fluid–bubble coupling force f_i^n, which is required to compute RU_i^n in (A 13) below, is evaluated using (2.8) and (A 10) as

$$f_i^n = -C^n\left(\frac{\mathrm{D}U_i^n}{\mathrm{D}t} - g_i\right). \tag{A 12}$$

(*c*) Time integration of (A 7), without the pressure-gradient term, is performed using the Adams–Bashforth scheme:

$$\frac{\hat{U}_i^* - U_i^n}{\Delta t} = \tfrac{3}{2}RU_i^n - \tfrac{1}{2}RU_i^{n-1}, \tag{A 13}$$

where $\hat{U}_i^*$ is the value of U_i^* before the pressure correction (A 18) is applied. The asterisk denotes the predicted value at time level $n+1$, i.e. the output of the predictor. The time step used is $\Delta t = \Delta x/256$ for the $96 \times 2 \times 96$ mesh.

(*d*) Time integration of (A 8) is performed according to

$$\frac{C^* - C^n}{\Delta t} = \tfrac{3}{2}RC^n - \tfrac{1}{2}RC^{n-1}. \tag{A 14}$$

(*e*) Time integration of (A 9) is performed according to

$$\frac{V^* - V_i^n}{\Delta t} = \tfrac{3}{2}RV_i^n - \tfrac{1}{2}RV_i^{n-1}. \tag{A 15}$$

(*f*) The following Poisson equation for pressure,

$$\nabla^2 P^* = \frac{1}{\Delta t}(\partial_i \hat{U}_i^* - \partial_i U_i^*), \tag{A 16}$$

written in finite-difference form (Gerz, Schumann & Elghobashi 1989) is solved using a two-dimensional fast Fourier transform (FFT) in each (x, y)-plane and Gaussian elimination in the z-direction (Schmidt, Schumann & Volkert 1984). In order to obtain the right-hand side of (A 16), $\partial_i \hat{U}_i^*$ is computed using a second-order central-difference scheme and $\partial_i U_i^*$ is evaluated using the continuity equation of the carrier fluid (2.4) as

$$\partial_i U_i^* = \partial_t C^* + \partial_i (CU_i)^* \simeq RC^* + \partial_i\left(C^* U_i^n\right). \tag{A 17}$$

(*g*) U_i^* is updated by accounting for the pressure correction as

$$U_i^* = \hat{U}_i^* - \Delta t\, \partial_i P^*. \tag{A 18}$$

Corrector The following seven steps (*a*) to (*g*) constitute the corrector.

(*a*) The Lagrangian derivatives of the fluid-velocity components, $\mathrm{D}U_i^*/\mathrm{D}t$, which are required to compute the coupling force f_i^* from (2.8) and RV_i^* from (A 6), are evaluated as

$$\frac{\mathrm{D}U_i^*}{\mathrm{D}t} = \partial_t U_i^* + \partial_j (U_i^* U_j^*) - U_i^* \partial_j U_j^*, \tag{A 19}$$

where

$$\partial_t U_i^* = \frac{U_i^* - U_i^n}{\Delta t}. \tag{A 20}$$

(*b*) The fluid–bubble coupling force f_i^*, which is required to compute RU_i^* in (A 22) below, is evaluated using (2.8) and (A 19) as

$$f_i^* = -C^*\left(\frac{\mathrm{D}U_i^*}{\mathrm{D}t} - g_i\right). \tag{A 21}$$

(*c*) Time integration of (A 7), without the pressure-gradient term, is performed using the Crank–Nicolson scheme:

$$\frac{\hat{U}_i^{n+1} - U_i^n}{\Delta t} = \tfrac{1}{2}\left(RU_i^* + RU_i^n\right), \tag{A 22}$$

where $\hat{U}_i^{n+1}$ is the value of U_i^{n+1} before the pressure correction (A 27) is applied.

(*d*) Time integration of (A 8) is performed according to

$$\frac{C^{n+1} - C^n}{\Delta t} = \tfrac{1}{2}(RC^* + RC^n). \tag{A 23}$$

(*e*) Time integration of (A 9) is performed according to

$$\frac{V^{n+1} - V_i^n}{\Delta t} = \tfrac{1}{2}\left(RV_i^* + RV_i^n\right). \tag{A 24}$$

(*f*) P^{n+1} is computed by solving the following Poisson equation:

$$\nabla^2 P^{n+1} = \frac{1}{\Delta t}\left(\partial_i \hat{U}_i^{n+1} - \partial_i U_i^{n+1}\right). \tag{A 25}$$

In order to obtain the right-hand side of (A 25), $\partial_i \hat{U}_i^{n+1}$ is computed using a second-order central-difference scheme and $\partial_i U_i^{n+1}$ is evaluated using the fluid-continuity equation (2.4) as

$$\partial_i U_i^{n+1} = \partial_t C^{n+1} + \partial_i (CU_i)^{n+1} \simeq RC^{n+1} + \partial_i (C^{n+1} U_i^*). \tag{A 26}$$

(*g*) U_i^{n+1} is updated by accounting for the pressure correction as

$$U_i^{n+1} = \hat{U}_i^{n+1} - \Delta t\, \partial_i P^{n+1}. \tag{A 27}$$

We ensure that the governing equations (2.4) and (A 7)–(A 9) are satisfied at each grid point of the computational mesh and at each time step by monitoring the residuals. The maximum and minimum values of the difference between the left-hand side and right-hand side in (A 7)–(A 9) computed instantaneously at each grid point of the computational mesh are of the order of 10^{-13}. The maximum and minimum values of the left-hand side of (2.4) are of the order of 10^{-7}, because of the approximation used in (A 17) and (A 26). Similarly the conservation of the bubble concentration C is satisfied at all times, as evidenced by the computed absolute value of the error $(C_0 - \langle C \rangle)/C_0$, which remains smaller than 10^{-14}. It should be noted that the Lagrangian–Eulerian mapping (LEM) method proposed by Druzhinin & Elghobashi (1998) for bubble-laden flow equations with one-way coupling is non-conservative.

Our results with two-way coupling show that the numerical solution obtained using only the predictor steps described above is stable in time until $C_m(t)$ reaches approximately 0.25. The additional corrector steps stabilize the solution in time until $C_m(t)$ reaches 0.5 (figure 16).

A.2. *One-way coupling*

The numerical algorithm for solving the governing equations of bubble-laden flow for one-way coupling, equations (2.11), (2.12), (2.6) and (2.7), differs from that of the two-way coupling described above as follows.

(i) The definition of RU_i, (A 4), becomes

$$RU_i \equiv -\partial_j (U_i U_j) + \nu\, \partial_j \partial_j U_i + g_i. \tag{A 28}$$

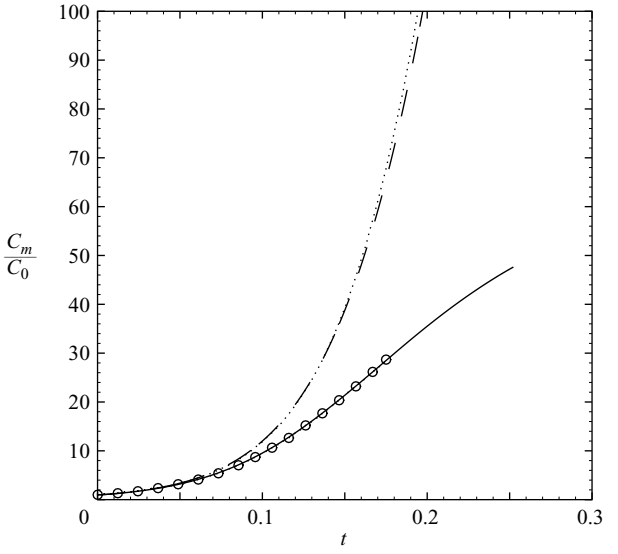

FIGURE 24. Temporal development of C_m/C_0 for case A using the two-fluid and Lagrangian methods with one-way and two-way coupling. Two-fluid, one-way (dashed line); two-fluid, two-way (solid line); Lagrangian, one-way (dotted line); Lagrangian, two-way (dotted line with circles).

(ii) In the Predictor steps (A 10) becomes

$$\frac{\mathrm{D}U_i^n}{\mathrm{D}t} = \partial_t U_i^n + \partial_j\left(U_i^n U_j^n\right) \tag{A 29}$$

and (A 12) is not computed.
In (f) the Poisson equation (A 16) becomes

$$\nabla^2 P^* = \frac{1}{\Delta t}\,\partial_i \hat{U}_i^*, \tag{A 30}$$

and (A 17) is not computed.

(iii) The corrector steps are not required since the numerical solution for one-way coupling is stable when performing only the predictor steps. Thus, the starred values of the predictor become the values at time level $n+1$.

Appendix B. Comparison of the two-fluid and Lagrangian approaches

Here we compare the results of the Lagrangian and two-fluid simulations of the bubble-laden TGV for case A (table 2). The governing equations and numerical method of the Lagrangian simulation are given by Ferrante & Elghobashi (2005; see § 2 and the Appendix). The main difference between the two-fluid and Lagrangian approaches is in the treatment of the dispersed phase. In the two-fluid (or Eulerian–Eulerian) approach the bubble phase is considered as a continuum, characterized by its instantaneous local concentration $C(\boldsymbol{x}, t)$ and its velocity $\boldsymbol{V}(\boldsymbol{x}, t)$. In the Lagrangian (or Eulerian–Lagrangian) approach the trajectory of each individual bubble is tracked in time; thus the dispersed phase is characterized by the bubble positions $\boldsymbol{x}_b(t)$ and velocities $\boldsymbol{V}_b(t)$. In the two-fluid formulation the local instantaneous bubble-phase concentration $C(\boldsymbol{x}, t)$ is advanced in time by solving the bubble-phase continuity equation (2.6), whereas in the Lagrangian formulation $C(\boldsymbol{x}, t)$ is computed from the

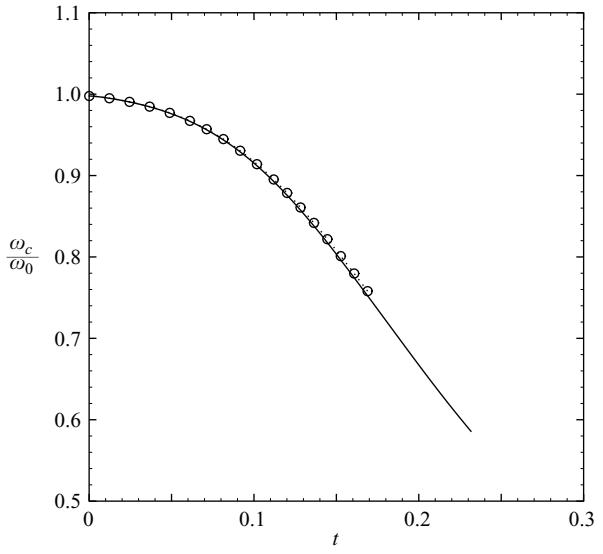

FIGURE 25. Temporal development of ω_c/ω_0 for case A using the two-fluid and Lagrangian methods with two-way coupling: two-fluid (solid line); Lagrangian (dotted line with circles).

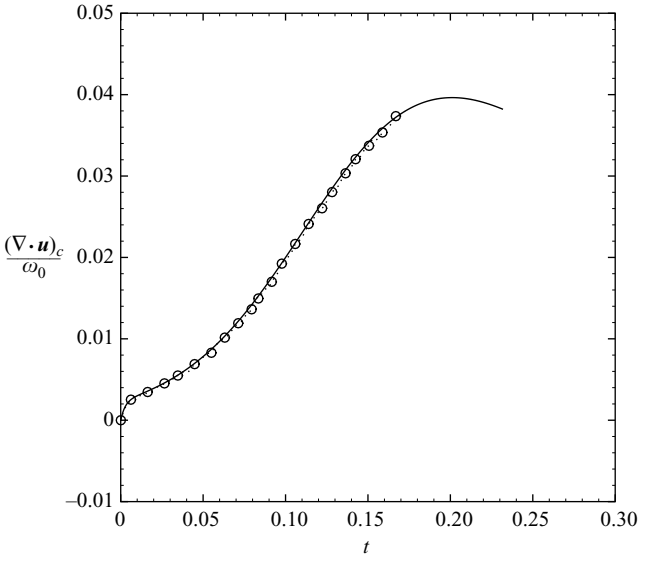

FIGURE 26. Temporal development of $(\nabla \cdot \boldsymbol{U})_c/\omega_0$ for case A using the two-fluid and Lagrangian methods with two-way coupling: two-fluid (solid line); Lagrangian (dotted line with circles).

local number of bubbles N_b in a given computational cell of volume $\mathscr{V}_c$ as

$$C(\boldsymbol{x}, t) = N_b(\boldsymbol{x}, t)\frac{\pi d_b^3}{6}\frac{1}{\mathscr{V}_c(\boldsymbol{x})}, \tag{B 1}$$

where d_b is the bubble diameter.

In order to be able to compare the results of the Lagrangian and two-fluid simulations, we use the same computational mesh ($96 \times 2 \times 96$ grid points) and

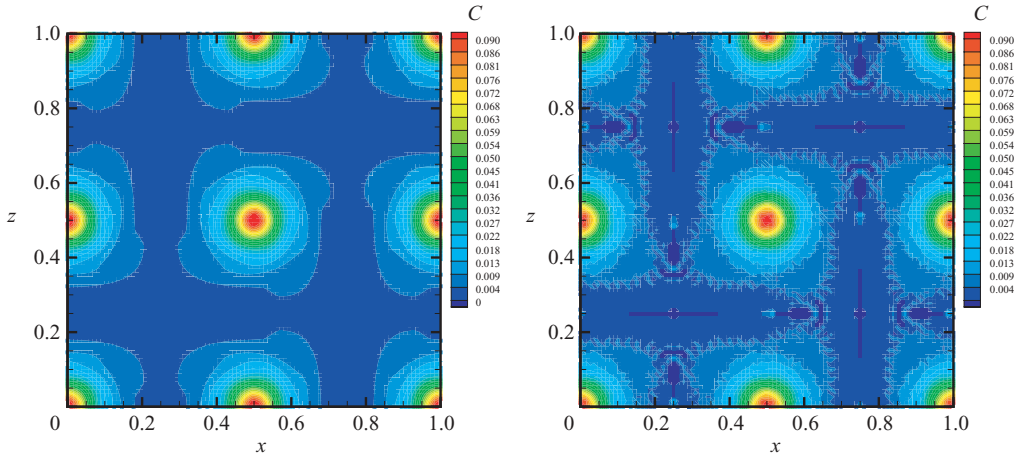

FIGURE 27. Instantaneous contours of the bubble concentration C at time $t = 0.1$ for case A (for two-way coupling): the two-fluid (left) and Lagrangian (right) approaches.

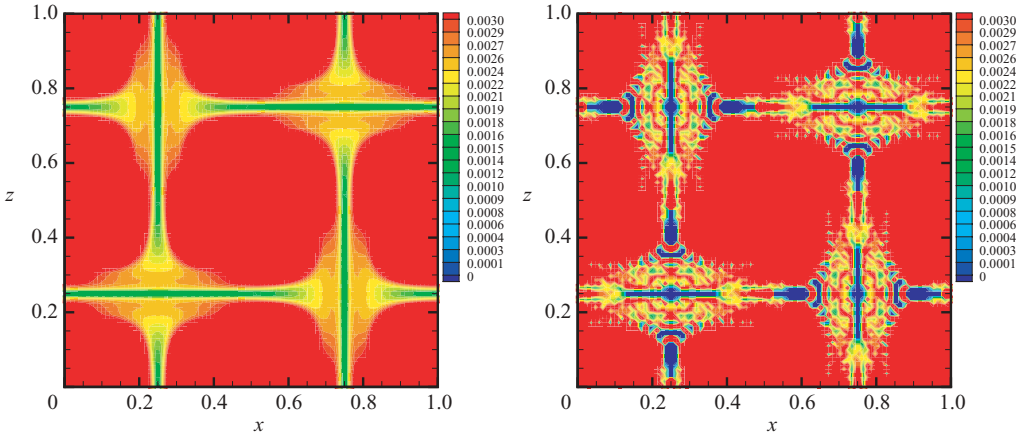

FIGURE 28. Instantaneous contours of the bubble concentration C at time $t = 0.1$ for case A (for two-way coupling) with a colour scale that differs from that in figure 27: the two-fluid (left) and Lagrangian (right) approaches.

prescribe the same initial conditions for both. For the Lagrangian simulation we release 460 800 bubbles (case A, table 2) with a uniform spatial distribution in the computational domain ($480 \times 2 \times 480$ bubbles in the x, y and z directions), such that the initial bubble-phase concentration is uniform and equal to 0.01 (case A), as in (2.15) for the two-fluid approach. We set each initial bubble-velocity component equal to that of the fluid at the bubble location, as in (2.14) for the two-fluid approach.

The temporal developments of C_m, $(\nabla \cdot \boldsymbol{U})_c$ and ω_c obtained from the two methods are nearly identical (figures 24–26). Since the CPU time of the Lagrangian simulation is 42 times that of the two-fluid simulation, the Lagrangian simulation was stopped at earlier times than the two-fluid simulation (figures 24–26). The instantaneous concentration fields obtained with the two methods are in excellent agreement (figure 27). However, in the regions where the local volume concentration is negligibly small the two-fluid method implicitly introduces a local smoothing at the numerical

grid scale. This limitation of the two-fluid approach is highlighted in figure 28, which shows that where the local concentration is small ($C < 0.003 < C_0 = 0.01$), e.g. in the neighbourhood of the zero-vorticity lines ($x = 0.25$), the two-fluid approach is unable to detect the absence of bubbles ($C_{min} = 0$ for the Lagrangian simulation, whereas $C_{min} = 0.0014$ for the two-fluid simulation) because of the smoothing out of the concentration field.

REFERENCES

Auton, T. R. 1987 The lift force on a spherical body in a rotational flow. *J. Fluid Mech.* **183**, 199–218.

Detsch, R. M. 1991 Small air bubbles in reagent grade water and seawater 1. Rise velocities of 20 to 1000-μm-diameter bubbles. *J. Geophys. Res.* **96** (C5), 8901–8906.

Djeridi, H., Gabillet, C. & Billard, J. Y. 2004 Two-phase Couette–Taylor flow: arrangement of the dispersed phase and effects on the flow structures. *Phys. Fluids* **16** (1), 128–139.

Drew, D. A. 1983 Mathematical modeling of two-phase flow. *Annu. Rev. Fluid Mech.* **15**, 261–291.

Drew, D. A. & Passman, S. L. 1999 *Theory of Multicomponent Fluids*. Springer.

Druzhinin, O. A. & Elghobashi, S. 1998 Direct numerical simulation of bubble-laden turbulent flows using the two fluid formulation. *Phys. Fluids* **10** (3), 685–697.

Druzhinin, O. A. & Elghobashi, S. E. 2001 Direct numerical simulation of a three-dimensional spatially developing bubble-laden mixing layer with two-way coupling. *J. Fluid Mech.* **429**, 23–61.

Ferrante, A. & Elghobashi, S. 2003 On the physical mechanism of two-way coupling in particle-laden isotropic turbulence. *Phys. Fluids* **15** (2), 315–329.

Ferrante, A. & Elghobashi, S. 2004 On the physical mechanisms of drag reduction in a spatially developing turbulent boundary layer laden with microbubbles. *J. Fluid Mech.* **503**, 345–355.

Ferrante, A. & Elghobashi, S. 2005 Reynolds number effect on drag reduction in a microbubble-laden spatially developing turbulent boundary layer. *J. Fluid Mech.* **543**, 93–106.

Gerz, T., Schumann, U. & Elghobashi, S. 1989 Direct numerical simulation of stratified homogeneous turbulent shear flows. *J. Fluid Mech.* **200**, 563–594.

Hirsch, C. 1990 *Numerical Computation of Internal and External Flows*, vol. 2. John Wiley & Sons.

Marchioro, M., Tanksley, M. & Prosperetti, A. 1999 Mixture pressure and stress in disperse two-phase flow. *Intl J. Multiphase Flow* **25**, 1395–1429.

Maxey, M. R. 1987*a* The gravitational settling of aerosol particles in homogeneous turbulence and random flow fields. *J. Fluid Mech.* **174**, 441–465.

Maxey, M. R. 1987*b* The motion of small spherical particles in a cellular flow field. *Phys. Fluids* **30** (7), 1915–1928.

Maxey, M. R. & Riley, J. 1983 Equation of motion for a small rigid sphere in a turbulent fluid flow. *Phys. Fluids* **26** (4), 883–889.

Mazzitelli, I. M., Lohse, D. & Toschi, F. 2003 On the relevance of the lift force in bubbly turbulence. *J. Fluid Mech.* **488**, 283–313.

Najm, H. N., Wyckoff, P. S. & Knio, O. M. 1998 A semi-implicit numerical scheme for reacting flow i. stiff chemistry. *J. Comput. Physics* **143** (2), 381–402.

Prosperetti, A. & Zhang, D. Z. 1995 Finite-particle-size effects in disperse tho phase flows. *Theoret. and Comput. Fluid Dynamics* **7**, 429–440.

Rightley, P. M. & Lasheras, J. C. 2000 Bubble dispersion and interphase coupling in a free-shear flow. *J. Fluid Mech.* **412**, 21–59.

Roe, P. L. 1985 Some contributions to the modelling of discontinuous flows. In *Proc. 1983 AMS-SIAM Summer Seminar on Large Scale Computing in Fluid Mechanics, Lectures in Applied Mathemathics*, vol. 22, pp. 163–193. SIAM, Philadelphia.

Ruetsch, G. & Meiburg, E. 1993 On the motion of small spherical bubbles in two-dimensional vortical flows. *Phys. Fluids* A **5** (10), 2326–2341.

Saffman, P. G. 1965 The lift on a small sphere in a slow shear flow. *J. Fluid Mech.* **22**, 385–400. Corrigendum P. G. Saffman *J. Fluid Mech.* 31, p. 624, 1968.

Schmidt, H., Schumann, U. & Volkert, H. 1984 Three dimensional, direct and vectorized elliptic solvers for various boundary conditions. *Rep.* 84-15. DFVLR-Mitt.

Sirignano, W. A. 2005 Volume averaging for the analysis of turbulent spray flows. *Intl J. Multiphase Flow* **31**, 675–705.

Sridhar, G. & Katz, J. 1999 Effect of entrained bubbles on the structure of vortex rings. *J. Fluid Mech.* **397**, 171–202.

Taylor, G. I. 1923 On the decay of vortices in a viscous fluid. *Philos. Mag.* **46**, 671–674.

Van Leer, B. 1979 Towards the ultimate conservative difference scheme. v. a second order sequel to Godunov's method. *J. Comput. Phys.* **32**, 101–136.

Wang, L. P. & Maxey, M. R. 1993 The motion of microbubbles in a forced isotropic and homoheneous turbulence. *Appl. Sci. Res.* **51**, 291–296.

Zhang, D. Z. & Prosperetti, A. 1997 Momentum and energy equations for disperse two-phase flows and their closure for dilute suspensions. *Intl J. Multiphase Flow* **23**, 425–453.